Orbital quantization of electronic states in a magnetic field as the origin of second-harmonic generation in diamagnetic semiconductors

I. Sänger,[1] D. R. Yakovlev,[1,2] B. Kaminski,[1] R. V. Pisarev,[2] V. V. Pavlov,[2] and M. Bayer[1]
[1]*Experimentelle Physik II, Universität Dortmund, 44221 Dortmund, Germany*
[2]*A. F. Ioffe Physical-Technical Institute, Russian Academy of Sciences, 194021 St. Petersburg, Russia*
(Received 13 June 2006; revised manuscript received 23 August 2006; published 25 October 2006)

Magnetic-field-induced second-harmonic generation (MFISH) has been studied in the III-V and II-VI diamagnetic semiconductors GaAs, CdTe, and (Cd,Mg)Te over broad spectral ranges and at temperatures varying from 6 to 200 K. The external magnetic field gives rise to time-reversal symmetry breaking, causing optical nonlinearities. A series of narrow MFISH lines has been observed in the spectral range near the band gap in magnetic fields up to 11 T. The magnetoexciton states associated with the optical transitions between Landau levels are responsible for the observed MFISH spectra. Orbital quantization of electronic states is therefore established as an origin of MFISH generation. The rotational anisotropy of the MFISH signal distinctly differs from that in the electric-dipole approximation. Model calculations, based on a phenomenological analysis using nonlocal contributions to the nonlinear optical susceptibility, reveal the importance of nonlinear magneto-optical spatial-dispersion, which acts together with the electric-dipole term.

DOI: 10.1103/PhysRevB.74.165208 PACS number(s): 75.50.Pp, 42.65.Ky, 71.70.Ej, 71.70.Di

I. INTRODUCTION

Since the invention of lasers, semiconductors have been probed by various nonlinear optical techniques, including second harmonic generation (SHG). SHG is one of the simplest nonlinear processes, but still can provide in addition to linear optics a lot of important information on the electronic and magnetic structure of solids.[1–3] This is primarily because the selection rules for the electronic transitions may radically differ in linear and nonlinear optics. Recent progress in the studies and applications of SHG can be found in literature.[4–8]

The invention of tunable optical parametric oscillators covering wide spectral ranges has strongly extended the experimental tools for on- and off-resonance studies of SHG. However, most of the earlier reports on SHG in semiconductors were restricted to narrow spectral ranges in the transparency region below the band gap. Only recently, reports on SHG at room temperature over wide spectral ranges below and above the band gap were made for ZnSe, ZnTe, ZnS,[9] and GaAs.[10] Theoretical studies of crystallographic SHG in semiconductors have been reported in several publications (see, e.g., Refs. 11–13). However, for semiconductors subject to magnetic fields such theoretical considerations are still missing.

Magneto-optical spectroscopy is an efficient method for studies of electronic and spin-related optical phenomena,[14–16] however experimental reports on magnetic-field-induced SHG (we adopt the abbreviation MFISH for this phenomenon as suggested in Refs. 17 and 18) and magnetization-induced SHG (MSHG) have remained scarce. In the early 1970s, SHG in InSb was studied below the energy gap using a single-wavelength CO_2 laser at 10.6 μm and tuning the energy gap by applying magnetic fields up to 5.5 T.[19] This study allowed absolute measurements of the coherence length as a function of magnetic field. A weak SHG response of a silicon surface to an applied magnetic field at a fixed laser frequency was reported in Ref. 20. Broad spectral features near the band gap related to magnetic ordering have been published for the ferromagnetic semiconductor (Ga,Mn)As (Ref. 21) and the diluted magnetic semiconductor (Cd,Mn)Te.[22] However, these studies did not allow clarification of the microscopic origins of the observed phenomena.

Very recently, a low-temperature spectroscopic study of diamagnetic GaAs in the vicinity of the band gap has disclosed a series of narrow MFISH lines with complicated rotational anisotropies.[23] It has been shown that the magnetic field breaks the time-inversion symmetry and induces different optical nonlinearities with well-defined polarization properties and characteristic magnetic-field and temperature dependencies. Orbital and spin quantization of electronic states have been suggested as possible microscopic origins for the MFISH phenomenon. Indeed, a follow-up study of the diluted magnetic semiconductor (Cd,Mn)Te has shown that MFISH in diamagnetic semiconductors, such as GaAs and CdTe, arises mainly due to orbital quantization,[23] whereas spin quantization is of major importance in paramagnetic semiconductors characterized by giant Zeeman spin splittings.[18]

A detailed study of the orbital quantization as origin of MFISH is chosen as topic for this paper. We address MFISH in magnetic fields up to 11 T for the diamagnetic zinc-blende semiconductors GaAs, CdTe, and (Cd,Mg)Te in the spectral range near their band gaps. To explain the observed phenomena, it is necessary to consider specific nonlinear processes for the interaction of the laser light with the medium, which is magnetized by an external magnetic field.

The paper is organized as follows. Section II introduces a phenomenological analysis and transformation properties of the nonlinear optical susceptibility in zinc-blende semiconductors with and without magnetic field. Experimental details are given in Sec. III. A comprehensive study of MFISH in GaAs is described in Secs. IV–VII. Then, after brief presentation of MFISH in CdTe in Sec. VIII, we turn to the sample quality impact on the MFISH spectra in Sec. IX.

II. POLARIZATION SELECTION RULES FOR SECOND HARMONIC GENERATION

In this section we consider the selection rules for different SHG processes that form the basis for the analysis of the rotational anisotropy of SHG signals. The analysis will be done for linearly polarized light. Since the crystallographic SHG process in the electric-dipole approximation is the simplest process, which in most cases provides the strongest contribution, it will be discussed first. However, our attention in this paper is focused on higher-order SHG processes induced by application of an external magnetic field (MFISH). In order to highlight them, experiments have been performed for specific sample orientations for which the crystallographic SHG is fully suppressed for symmetry reasons.

The zinc-blende semiconductors discussed in this paper are described by the non-centro-symmetric point group $\bar{4}3m$. From the symmetry point of view, the leading-order SHG polarization $\mathbf{P}(2\omega)$ in the electric-dipole approximation[1–3] can be written as

$$P_i(2\omega) = \epsilon_0 \chi_{ijk}(2\omega) E_j(\omega) E_k(\omega), \tag{1}$$

describing the crystallographic contribution to SHG, where $\mathbf{E}(\omega)$ is the electric field at the fundamental frequency and ϵ_0 is the vacuum permittivity. Microscopically χ_{ijk} is given by the non-centro-symmetric part of the electric charge density. It is a polar third-rank tensor with nonvanishing components[2,3,24]

$$\chi_{xyz} = \chi_{xzy} = \chi_{yxz} = \chi_{yzx} = \chi_{zxy} = \chi_{zyx}, \tag{2}$$

where x, y, and z denote the crystallographic axes.

In the following the polarization dependence of the SHG signal and, in particular, its rotational anisotropy, are calculated for different experimental geometries. To that reason, the tensor components given by Eq. (2) are transformed from the crystal coordinate system into the coordinate system of the laser light beam, which depends on the experimental geometry. Afterward they are inserted into Eq. (1). The coordinate system of light is given by the wave vectors $\mathbf{k}(\omega) \| \mathbf{k}(2\omega)$ and the electric field vectors $\mathbf{E}(\omega)$ and $\mathbf{E}(2\omega)$ of the fundamental and the second harmonic (SH) light. The crystallographic coordinate system is defined by the x, y, and z axes.

First, the rotational anisotropy for a (110) sample orientation and normal light incidence with $\mathbf{k} \| [110]$ has been calculated. The results are given in Fig. 1. For convenience in presentation, light propagating along the $[10\bar{1}]$ axis, which is an equivalent axis to [110], is considered. For the polarization geometry $\mathbf{E}(2\omega) \| \mathbf{E}(\omega)$, the SHG anisotropy is given by

$$I(2\omega)_{\|}^{\mathrm{SHG}} \propto |\chi_{xyz}(\cos\vartheta - \cos 3\vartheta)|^2. \tag{3}$$

For $\mathbf{E}(2\omega) \perp \mathbf{E}(\omega)$

$$I(2\omega)_{\perp}^{\mathrm{SHG}} \propto \left|\chi_{xyz}\left(-\tfrac{1}{3}\sin\vartheta + \sin 3\vartheta\right)\right|^2 \tag{4}$$

is derived. In Eqs. (3) and (4), the rotational anisotropy is given as a function of the angle ϑ between the polarization plane of the fundamental light and the crystallographic axis [010].

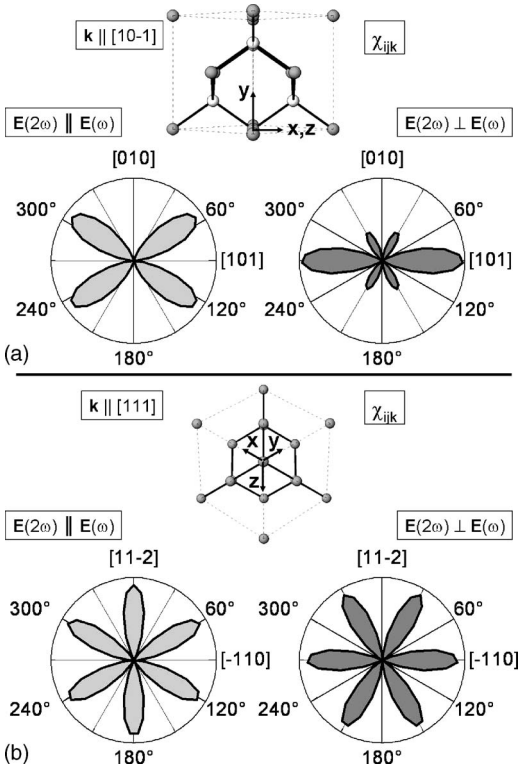

FIG. 1. Simulations of the crystallographic SHG rotational anisotropy for geometries $\mathbf{E}(2\omega) \| \mathbf{E}(\omega)$ and $\mathbf{E}(2\omega) \perp \mathbf{E}(\omega)$ for (110) $\equiv (10\bar{1})$ and (111) crystal orientations, based on Eqs. (3)–(6). $\mathbf{k}$ is oriented perpendicular to the figure plane along the crystallographic axis $[10\bar{1}]$ and [111] in (a) and (b), respectively.

For another geometry, considering a (111) crystal orientation with light propagating along the [111] axis, the SHG anisotropy is described by

$$I(2\omega)_{\|}^{\mathrm{SHG}} \propto |\chi_{xyz} \cos 3\theta|^2 \tag{5}$$

in the case of $\mathbf{E}(2\omega) \| \mathbf{E}(\omega)$, and

$$I(2\omega)_{\|}^{\mathrm{SHG}} \propto |\chi_{xyz} \sin 3\theta|^2 \tag{6}$$

is obtained for $\mathbf{E}(2\omega) \perp \mathbf{E}(\omega)$. Here, the rotational anisotropy is given as a function of the angle θ between the polarization plane of the fundamental light and the crystallographic axis $[11\bar{2}]$. Figure 1 shows simulations of the crystallographic SHG anisotropy using Eqs. (3)–(6).

For (001)-oriented samples, the χ_{ijk} components do not provide crystallographic SHG for normal light incidence. This property allows one to study MFISH signals avoiding their interference with crystallographic ones.

Let us turn now to the analysis of MFISH signals for (001) crystal orientation and normal light incidence with $\mathbf{k} \| [001]$. The leading order SHG contribution in a static magnetic field $\mathbf{H} \equiv \mathbf{H}(0)$, which has to be distinguished from the $\mathbf{H}(\omega)$ of the light field, can be described by

$$P_i(2\omega) = \epsilon_0 i \chi_{ijkl} E_j(\omega) E_k(\omega) H_l. \tag{7}$$

This contribution is related to perturbations of the charge and spin distribution by the external magnetic field. The

magnetic-field-induced nonlinear susceptibility χ_{ijkl} is an axial fourth-rank i-tensor with nonvanishing components[24–26]

$$-\underline{\chi_{xyyx}} = \chi_{xzzx} = \chi_{yxxy} = -\chi_{yzzy} = -\chi_{zxxz} = \chi_{zyyz},$$

$$-\chi_{xyxy} = \chi_{xzxz} = \underline{\chi_{yxyx}} = -\chi_{yzyz} = -\chi_{zxzx} = \chi_{zyzy},$$

$$-\chi_{xxyy} = \chi_{xxzz} = \underline{\chi_{yyxx}} = -\chi_{yyzz} = -\chi_{zzxx} = \chi_{zzyy}. \quad (8)$$

The analysis of these tensor components χ_{ijkl} shows that the MFISH given by Eq. (7) is forbidden in the Faraday geometry $\mathbf{k}\|\mathbf{H}$.[27] Without loss of generality one can select the magnetic field direction along the z axis ($\mathbf{H}\|\mathbf{z}$). In this case, only tensor components with the last index $l=z$ contribute. On the other hand, due to experimental geometry $\mathbf{k}\|\mathbf{z}$, the first three indices cannot be equal to z $(i,j,k\neq z)$. No such components appear, however, in Eq. (8), where only even combination of indices are present.

For the Voigt geometry $\mathbf{k}\perp\mathbf{H}$, especially for $\mathbf{k}\|\mathbf{z}$ and $\mathbf{H}\|\mathbf{x}$, only the underlined tensor components in Eq. (8) contribute to the SHG signal. Because of the permutability of the two exciting photons, the components $\chi_{yxyx}=\chi_{yyxx}$ are identical. Therefore, only two tensor components χ_{xyyx} and χ_{yxyx} are independent. Using Eq. (7) for the MFISH polarization and applying a transformation of the coordinate system, the MFISH rotational anisotropy can be calculated. In the case of $\mathbf{E}(2\omega)\|\mathbf{E}(\omega)$ the anisotropy is given by

$$I(2\omega)_{\|}^{\mathrm{MFISH}} \propto |-(\chi_{xyyx}+2\chi_{yxyx})(\sin\varphi+\sin 3\varphi)|^2, \quad (9)$$

and for $\mathbf{E}(2\omega)\perp\mathbf{E}(\omega)$

$$I(2\omega)_{\perp}^{\mathrm{MFISH}} \propto |\chi_{xyyx}(3\cos\varphi+\cos 3\varphi)+\chi_{yxyx}(-2\cos\varphi + 2\cos 3\varphi)|^2 \quad (10)$$

is derived for light propagating along the [001] axis. Here the MFISH intensity is given as a function of the angle φ between the polarization plane of the fundamental light and the crystallographic [010] axis. Figure 2 shows the rotational anisotropy for the specific choice of tensor components $-\chi_{xyyx}=\chi_{yxyx}$. Note that the shape of the anisotropy pattern for $I(2\omega)_{\|}^{\mathrm{MFISH}}$ in Eq. (9) does not depend on the choice of values for χ_{xyyx} and χ_{yxyx}. In contrast, the shape of the anisotropy pattern for $I(2\omega)_{\perp}^{\mathrm{MFISH}}$ in Eq. (10) varies with the choice of values for χ_{xyyx} and χ_{yxyx}.

Our previous studies of MFISH (Ref. 18 and 23) have shown that the electric dipole approximation is not sufficient to model the experimental findings for semiconductors with zinc-blende structure, such as GaAs, CdTe, and (Cd,Mn)Te. To solve this problem, higher-order terms of the nonlinear susceptibility have to be taken into account.

In general, the MFISH contributions can be written as

$$\begin{pmatrix}\mathbf{P}^{2\omega}\\ \mathbf{M}^{2\omega}\\ \mathbf{Q}^{2\omega}\end{pmatrix} \propto \begin{pmatrix}\chi^{eeem} & \chi^{eemm} & \chi^{emmm}\\ \chi^{meem} & \chi^{memm} & \chi^{mmmm}\\ \chi^{qeem} & \chi^{qemm} & \chi^{qmmm}\end{pmatrix}\begin{pmatrix}\mathbf{E}^{\omega}\mathbf{E}^{\omega}\mathbf{H}\\ \mathbf{E}^{\omega}\mathbf{H}^{\omega}\mathbf{H}\\ \mathbf{H}^{\omega}\mathbf{H}^{\omega}\mathbf{H}\end{pmatrix}, \quad (11)$$

where $\mathbf{H}^{\omega}\equiv\mathbf{H}(\omega)$ is the magnetic field at the fundamental frequency and $\mathbf{M}^{2\omega}\equiv\mathbf{M}(2\omega)$ as well as $\mathbf{Q}^{2\omega}\equiv\mathbf{Q}(2\omega)$ are the magnetization and the electric-quadrupole polarization at the MFISH frequency, respectively. All nonlinear susceptibilities contributing to Eq. (11) are symmetry allowed for the point group $\bar{4}3m$.[24] However, nonlinear processes, which include more than two magnetic quantities, such as χ^{emmm}, χ^{memm}, χ^{mmmm}, and χ^{qmmm} or involve both an electric-quadrupole polarization and a magnetic quantity such as χ^{qemm} will be neglected in the following since they are believed to be small. The remaining contributions χ^{eemm}, χ^{meem}, and χ^{qeem}, which involve either two magnetic quantities or an electric-quadrupole polarization, can be rewritten as

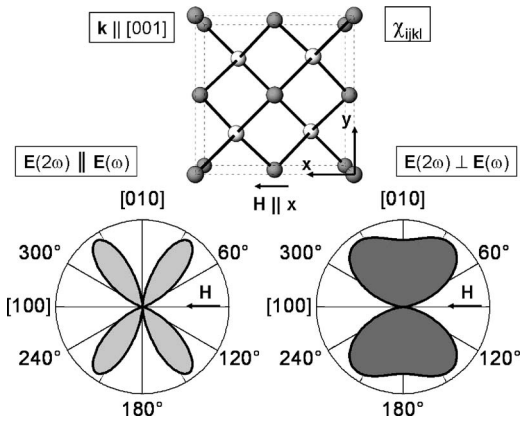

FIG. 2. Simulations of the MFISH rotational anisotropy for the geometries $\mathbf{E}(2\omega)\|\mathbf{E}(\omega)$ and $\mathbf{E}(2\omega)\perp\mathbf{E}(\omega)$ for (001) crystal orientation, based on Eqs. (9) and (10) taking into account the electric-dipole approximation. Light wave vector $\mathbf{k}\|[001]$ and external magnetic field $\mathbf{H}\|[100]$.

$$P_i(2\omega) = \epsilon_0\chi_{ijklm}E_j(\omega)E_k(\omega)k_l(\omega)H_m, \quad (12)$$

so that nonlinear magneto-optical spatial-dispersion is taken into account. The appearance of the wave vector $\mathbf{k}(\omega)$ arises from the multipole expansion of the vector potential up to the first order, given by

$$\mathbf{A} = A_0\mathbf{e}\cdot\exp[\pm i\mathbf{k}(\omega)\mathbf{r}] \approx A_0\mathbf{e}[1\pm i\mathbf{k}(\omega)\mathbf{r}], \quad (13)$$

where $\mathbf{e}$ is the polarization unit vector and A_0 is the amplitude of the vector potential. The term $A_0\mathbf{e}$ leads to the electric-dipole SHG contribution considered in Eqs. (1) and (7). The next order term $A_0\mathbf{e}i\mathbf{k}(\omega)\mathbf{r}$ represents both the magnetic-dipole and the electric-quadrupole approximations, leading to the $i\mathbf{k}$ dependence of the MFISH contributions described by Eq. (12).

The nonlinear susceptibility tensor χ_{ijklm} is an axial time-invariant fifth-rank tensor. The full set of nonvanishing tensor components is given by Eq. (A1) in the Appendix. The analysis of the tensor components shows that the MFISH described by Eq. (12) is forbidden in the Faraday geometry ($\mathbf{k}\|\mathbf{H}\|\mathbf{z}$), since tensor components of type χ_{ijklm} with $i,j,k\neq z$ and $l,m=z$ are not allowed.

The tensor components which provide MFISH in the Voigt geometry with $\mathbf{k}\|\mathbf{z}$ and $\mathbf{H}\|\mathbf{x}$ are given by

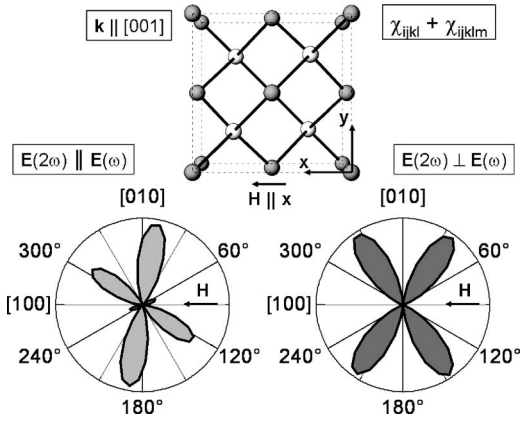

FIG. 3. Simulations of the MFISH rotational anisotropy for the geometries $\mathbf{E}(2\omega)\|\mathbf{E}(\omega)$ and $\mathbf{E}(2\omega)\perp\mathbf{E}(\omega)$ for (001) crystal orientation according to Eqs. (15) and (16), taking into account the electric-dipole terms as well as the spatial dispersion terms ($\mathbf{k}\|[001]$). The following parameters have been chosen based on the results of Ref. 23: $\chi_{xyyx}=3$, $\chi_{yxyx}=3$, $\chi_{yxxzx}=8$, $\chi_{xxyzx}=1$, and $\chi_{yyyzx}=170$.

$$\chi_{yxxzx},\ \chi_{yyyzx},\ \chi_{xxyzx}=\chi_{xyxzx}. \tag{14}$$

Only the components χ_{yxxzx}, χ_{xxyzx}, and χ_{yyyzx} are independent. Using Eqs. (7) and (12) for the MFISH polarization and applying a transformation of the coordinate system, the MFISH rotational anisotropy can be calculated for the case when the electric-dipole *and* spatial-dispersion MFISH are included. For $\mathbf{E}(2\omega)\|\mathbf{E}(\omega)$ the anisotropy is given by

$$I(2\omega)_{\|}^{\mathrm{MFISH}} \propto |-(\chi_{xyyx}+2\chi_{yxyx})(\sin\varphi+\sin 3\varphi)+(\chi_{yxxzx} +2\chi_{xxyzx})(\cos\varphi-\cos 3\varphi)+\chi_{yyyzx}(3\cos\varphi +\cos 3\varphi)|^2, \tag{15}$$

and for $\mathbf{E}(2\omega)\perp\mathbf{E}(\omega)$

$$I(2\omega)_{\perp}^{\mathrm{MFISH}} \propto |\chi_{xyyx}(3\cos\varphi+\cos 3\varphi)+\chi_{yxyx}(-2\cos\varphi +2\cos 3\varphi)+\chi_{yxxzx}(3\sin\varphi-\sin 3\varphi) -\chi_{xxyzx}(2\sin\varphi+2\sin 3\varphi)+\chi_{yyyzx}(\sin\varphi +\sin 3\varphi)|^2 \tag{16}$$

is derived for light propagating along the [001] axis. The MFISH intensities shown in Fig. 3 are given as function of the angle φ between the polarization plane of the fundamental light and the crystallographic axis [010]. The specific values chosen for the tensor components to simulate the rotational anisotropy are given in the caption.

The MFISH rotational anisotropy in Fig. 3 was calculated for a (001) sample orientation, where the crystallographic SHG does not provide any contribution. In case of (110) or (111) sample orientations MFISH can be also observed, but it comes together with the crystallographic SHG, which is about an order of magnitude stronger than the MFISH. In order to avoid possible interference effects between MFISH and crystallographic SHG, an exact (001) sample orientation is used for the following experimental studies of MFISH.

Here a macroscopic model based on a symmetry analysis has been given. In the experimental part of this work, the effect of magnetic field, sample temperature, detection energy, and polarization direction onto the MFISH intensity is studied. For example, the rotational anisotropy for a certain electronic transition is considered as function of the magnetic field at a fixed temperature. In general, a variation of experimental conditions may lead to strong changes of the shape of the rotational anisotropy pattern. For an arbitrary angle φ, the MFISH intensity $I(2\omega)_{\|,\perp}^{\mathrm{MFISH}}(\varphi)$ is given by a superposition of all five tensor components and is described by Eqs. (15) and (16). Special cases are

$$I(2\omega)_{\|}^{\mathrm{MFISH}}(\varphi=0^\circ)\propto|\chi_{yyyzx}|^2 \tag{17}$$

$$I(2\omega)_{\perp}^{\mathrm{MFISH}}(\varphi=90^\circ)\propto|\chi_{yxxzx}|^2 \tag{18}$$

$$I(2\omega)_{\perp}^{\mathrm{MFISH}}(\varphi=0^\circ)\propto|\chi_{xyyx}|^2, \tag{19}$$

where the MFISH intensity is not determined by a superposition of several tensor components, but is reduced to a single component. The magnetic field dependence for $I(2\omega)_{\|}^{\mathrm{MFISH}}(0^\circ)\propto|\chi_{yyyzx}|^2$ was discussed in Ref. 23 for GaAs, where it was labeled χ_{yyyx} in the presentation of experimental results. The present work goes beyond the previous studies as it provides an in-depth analysis of the different MFISH tensor components for several semiconductors.

III. EXPERIMENT

The experimental setup for the SHG measurements is based on a solid-state Nd:YAG laser generating 8 ns pulses at a frequency of 10 Hz and a wavelength of 1064 nm (photon energy 1.17 eV). The laser light is transformed into the second (532 nm) and, subsequently, third (355 nm) optical harmonics by means of a KDP (KH_2PO_4) nonlinear crystal and is used to pump an optical parametric oscillator (OPO) with a BBO (β-BaB_2O_4) crystal. The OPO serves as light source in the spectral range of 0.6–1.6 eV, thus allowing for measurement of SHG spectra from 1.2 to 3.2 eV. The line width of the OPO emission is ~1 meV, limiting the spectral resolution of the setup. The fundamental frequency light generated by the OPO is linearly polarized. In most experiments reported here, linear polarization was chosen for both the fundamental and SH frequency. To measure the rotational anisotropy of the SHG signal, a Glan-Thompson prism and a half-wave plate were used to set the required orientation of the polarization planes of fundamental and frequency doubled photons. In a few cases, the SHG signal was excited and detected by photons circularly polarized by achromatic quarter-wave plates.

The experiments were performed mostly in transmission geometry. The fundamental photons passed through the studied samples inducing the SHG signal, which thereafter was detected by a liquid-nitrogen-cooled charge-coupled-device (CCD) camera. Optical filters were used to separate the fundamental and the SHG light. To suppress luminescence, which is strong for the studied semiconductors at low temperatures, a double pass prism monochromator with a reso-

lution of 2–10 nm was used. The measured SHG signals were normalized by the squared pulse energy of the light transmitted through the sample at the fundamental frequency. Very similar SHG signals but with lower intensity can be detected also in reflection, as shown below. It is worthwhile to note that no noticeable temperature rise of the crystal lattice was detected under laser illumination.

A split-coil solenoid with a temperature variable sample chamber was used for cooling the studied crystals. The sample was either in contact with pumped liquid helium at a temperature of 2 K or held in exchange gas in the temperature range from 6 to 200 K. Magnetic fields up to 11 T were applied either in the Voigt geometry perpendicular to the direction of light propagation or in the Faraday geometry parallel to the light propagation. For (001)-oriented samples the field was applied along the [110] axis in the Voigt configuration. An orthogonal configuration with an exact 90° angle between light propagation and magnetic field direction was chosen with high accuracy to ensure suppression of Faraday rotation of the fundamental beam polarization in the sample.

We studied GaAs samples fabricated by three different methods: (i) a 10 μm gas-phase-epitaxy layer grown on a semi-insulating GaAs (001) substrate,[28] (ii) a 2 μm epilayer grown by molecular-beam epitaxy on (001) GaAs substrate, and (iii) a (001)-oriented 0.5 mm thick platelet of bulk GaAs grown by the Bridgman method. The thicknesses of the GaAs substrates were ~500 μm for samples (i) and (ii). The type (i) sample had a very low defect density of 10^{14} cm^{-3} and most of experimental data presented here were collected on this sample. The samples of type (ii) and (iii) had defect densities of ~10^{15} cm^{-3}. They show experimental data very similar to sample (i), but with weaker and broader spectral features. A comparative study of these samples is given in Sec. IX.

II–VI semiconductor samples were fabricated by molecular-beam epitaxy on hybrid substrates consisting of 500 μm thick (001) GaAs overgrown by 3 μm of $Cd_{0.72}Mg_{0.28}Te$. Some 1 μm thick epilayers of the material of interest were grown on top of $Cd_{0.8}Mg_{0.2}Te$ buffer layers and were overgrown by a 50 nm $Cd_{0.8}Mg_{0.2}Te$ cap layer to reduce undesired surface effects. Three samples were studied with epilayers of CdTe (121304D), $Cd_{0.99}Mg_{0.01}Te$ (102805C), and $Cd_{0.92}Mg_{0.08}Te$ (102805A). The band gap, E_g, in this series of $Cd_{1-x}Mg_xTe$ increases with higher Mg content, following the dependence $E_g=(1.606+1.755x)$ eV. Accordingly, the buffer, cap, and hybrid substrate layers were transparent at the energies of the fundamental light, and the cap layer was transparent for the second harmonic signals.

IV. CRYSTALLOGRAPHIC SHG IN GaAs

As shown in Sec. II, for (001)-oriented cubic crystals the crystallographic SHG vanishes for normal light incidence. Therefore, for measuring this SHG contribution, the GaAs samples were tilted by 45° about the [010] axis. Note that the internal angle for the light propagation is significantly smaller than 45° due to the refractive index of GaAs, which

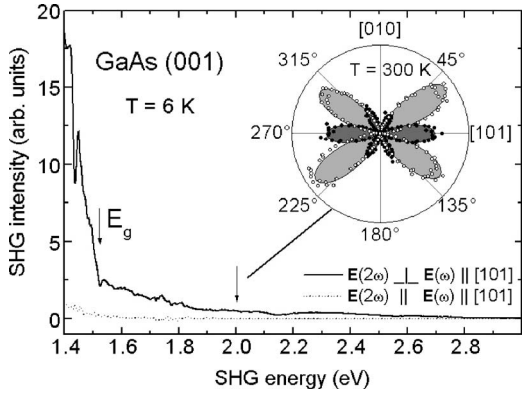

FIG. 4. Spectral dependence of the crystallographic SHG in the GaAs sample (i) tilted by 45° about the [010] axis. SHG spectra at $T=6$ K are shown for the electric-dipole allowed $\mathbf{E}(2\omega)\perp\mathbf{E}(\omega)\|[101]$ and forbidden $\mathbf{E}(2\omega)\|\mathbf{E}(\omega)\|[101]$ polarization geometries. The inset shows the rotational anisotropy detected at an energy of 2.0 eV for $T=300$ K in the two geometries: $\mathbf{E}(2\omega)\|\mathbf{E}(\omega)$ (light gray shaded area and open dots) and $\mathbf{E}(2\omega)\perp\mathbf{E}(\omega)$ (dark gray shaded area and filled dots).

varies strongly with wavelength.[29] However a variation of the internal angle does not change the shape of the rotational anisotropy pattern, but influences only the SHG intensity. Crystallographic SHG measured over a wide spectral range below and above the fundamental band gap $E_g=1.519$ eV is shown in Fig. 4. The vanishing of the signal for specific polarizations, which is clearly seen in the rotational anisotropy diagram, confirms that the signal is solely due to the SHG process and has no luminescence contribution. Luminescence is an optical process of lower order as compared to SHG and expected to display isotropic signals in cubic materials.

In the geometry $\mathbf{E}(2\omega)\perp\mathbf{E}(\omega)\|[101]$, a strong decrease of the SHG intensity was found around the band gap energy. This decrease does not display the pure spectral dependence of the squared nonlinear optical susceptibility given by Eq. (1). One of the reasons for that is reabsorption of the SHG light for energies exceeding the GaAs band gap. Another reason is the energy dependence of the SHG coherence length. It decreases continuously with increasing energy, both below and above the band gap. Below the band gap, the coherence length at normal incidence can be calculated as $l_{\mathrm{coh}}=\lambda/(4|n(\omega)-n(2\omega)|)$,[30] where λ is the fundamental light wavelength and $n(\omega)$ as well as $n(2\omega)$ are the refractive indices at the fundamental and second harmonic frequencies, respectively. From the values for the refractive index at 6 K the coherence length decreases from ~2 μm at 1.3 eV to ~1 μm at 1.5 eV. Above the band gap, the coherence length is reduced to the value of the attenuation length given by $l_{\mathrm{coh}}=1/\beta=\lambda/(2\pi k)$, where β is the imaginary part of the wave vector above the band gap and k is the absorption coefficient.[2] Estimates show that the coherence length decreases from ~1 μm at 1.6 eV to ~0.7 μm at 2 eV.

A fit of the experimental SHG anisotropy using Eqs. (3) and (4) is shown in the inset of Fig. 4. Note that the shape of the crystallographic anisotropy does not vary with SHG energy or with temperature. Good agreement between experi-

mental data and simulations (shaded areas) is observed confirming a high structural and optical quality of the sample as well as its proper orientation, as a misalignment larger than 1° between the crystallographic axes and the laboratory coordinate system would cause an observable distortion of the SHG rotational anisotropy patterns. Therefore, the rotational anisotropy of the SHG signal was used to control proper orientation of the samples.

V. MAGNETIC-FIELD-INDUCED SHG IN GaAs

For the rest of the paper we will concentrate on MFISH. The crystallographic contribution to the SHG signal due to χ_{ijk} has been suppressed using normal light incidence for (001)-oriented samples. This enables the detection of pure MFISH signals.

A. Faraday geometry

We start the presentation of the MFISH experimental data with the Faraday geometry $\mathbf{H}\|\mathbf{k}(\omega)\|\mathbf{z}$. The symmetry considerations using Eqs. (7) and (12) suggest that MFISH in this case is not allowed. In contrast, we do observe a set of SHG transitions induced by the external magnetic field, whose energy shifts with H coincide with the dispersion of magnetoexcitons in GaAs.[31,32] Possible explanations for this discrepancy will be given in Sec. VII A.

MFISH spectra measured with circularly polarized excitation are given in Fig. 5(a) for different magnetic fields. No signal is detected at zero magnetic field. With increasing field, a set of narrow lines shifting to higher energies shows up and gains in intensity. The energetically lowest peak shows the strongest intensity among all lines. It is labeled X, and we will show below that it can be assigned to the 1s-exciton state. We will also show (see Fig. 11) that MFISH lines are observable in the Faraday geometry in a spectral range up to 1.70 eV.

The magnetic field dependence of the peak energies is plotted in Fig. 5(b), where the symbol sizes are scaled by the MFISH intensity. The results appearance is typical for the fan-chart diagram of magnetoexcitons measured by linear optical spectroscopy techniques, such as absorption, reflection, or photoluminescence excitation. The shift of the lowest line shows good agreement with the diamagnetic shift of the 1s exciton state in GaAs,[32] which is indicated by the dashed line converging to 1.516 eV at zero field. The exciton binding energy in GaAs is 4.2 meV, and the band gap, which corresponds to optical transitions from the top of the valence band to the bottom of the conduction band has an energy of 1.519 eV at a temperature of 6 K. A calculation of the magnetoexciton spectrum is beyond the scope of this paper. Instead we plot in Fig. 5(b) the energies of the optical transitions between Landau levels[33] of free electrons and holes by solid lines. The magnetoexciton state energies are expected to be a few millielectron volts below the free particle energies due to the Coulomb attraction. The Landau-level transition energies have been calculated by

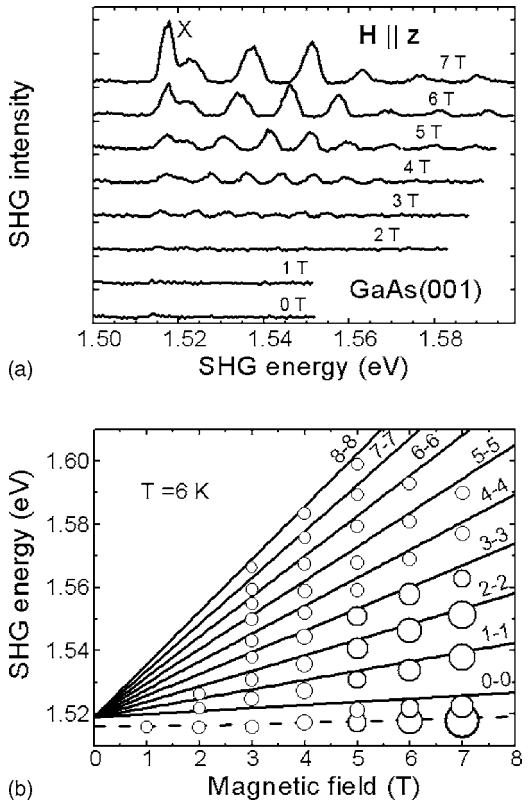

FIG. 5. (a) MFISH spectra in GaAs for Faraday geometry $\mathbf{H}\|\mathbf{k}(\omega)\|\mathbf{z}$ at different magnetic fields. Circular σ^- polarized light was chosen for excitation and detection. (b) Landau-level fan diagram of MFISH peak energies. Circles are experimental data with symbol sizes scaled by the MFISH intensity. Reasonable agreement is found between peak energies and optical Landau-level transition energies between calculated from Eq. (20) for $N_e=N_h$ (solid lines). The dashed line gives the literature data for the diamagnetic shift of the 1s-exciton state.

$$E = E_g + \frac{e\hbar}{c}\left[\frac{\frac{1}{2}+N_e}{m_e^*} + \frac{\frac{1}{2}+N_h}{m_h^*}\right]H, \tag{20}$$

where $E_g=1.519$ eV is the GaAs band gap energy, $m_e^*=0.067m_0$ and $m_{hh}^*=0.51m_0$ are the electron and heavy-hole effective masses,[34] and $N_e=N_h=0,1,2,\ldots$ are the Landau-level quantum numbers. Here, the Zeeman spin splitting of the Landau levels is not taken into account since in magnetic fields up to 7 T it does not exceed 1 meV, which is below the experimental resolution of our setup. As expected, the comparison between experiment and calculations reveals that the MFISH transitions are 2–5 meV below the calculated Landau-level transition energies so that the observed features can be indeed assigned to magnetoexciton states.

B. Voigt geometry

According to the analysis in Sec. II, MFISH is allowed in the Voigt geometry $(\mathbf{H}\|\mathbf{x},\mathbf{k}(\omega)\|\mathbf{z})$ both for the electric-dipole and magneto-optical spatial-dispersion approximations in Eqs. (7) and (12), respectively. This is in good agreement with the experimental data shown in Fig. 6(a). The

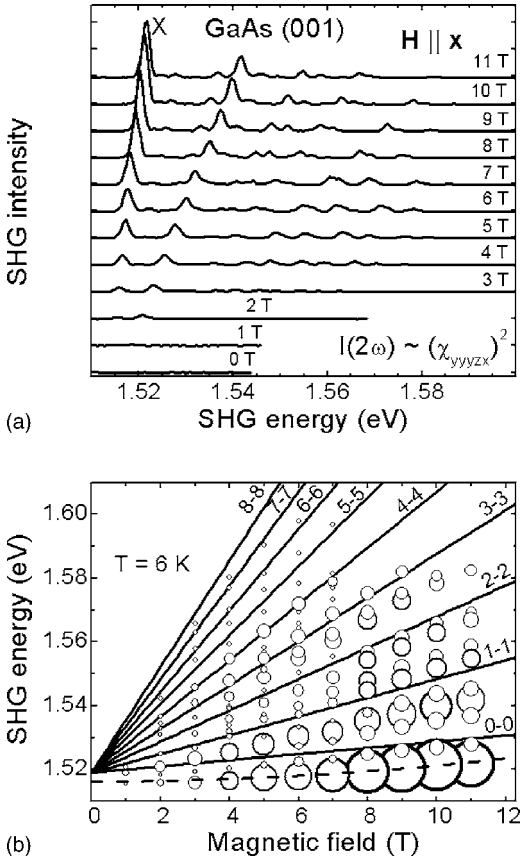

FIG. 6. (a) GaAs MFISH spectra at different magnetic fields (Voigt geometry). (b) Landau-level fan diagram of MFISH peak energies. Circles are experimental data with symbol sizes scaled by the MFISH intensity. Solid lines present optical transitions between Landau-levels calculated from Eq. (20) for $N_e=N_h$. The dashed line gives the literature data for the diamagnetic shift of the 1*s*-exciton state.

observed MFISH signal originates from the strongest component χ_{yyyzx} in the susceptibility tensor. The MFISH was measured for $\mathbf{E}(2\omega)\|\mathbf{E}(\omega)\|\mathbf{y}$ in magnetic fields up to 11 T. It is about five times more intense than the MFISH in the Faraday geometry (for details, see Fig. 11). Other experimental features are qualitatively similar to those found for the Faraday geometry: With increasing magnetic field a set of narrow lines appears that gain in intensity and shift to higher energies. Their energies, being compared to the calculated Landau-level fan-chart in Fig. 6(b), demonstrate good agreement for the two geometries. The main difference lies in the more complex peak structure for each Landau-level transition in the Voigt-geometry. This diversity originates from the field induced mixing of magnetoexciton states due to the complex energy and spin structure of the valence band. This phenomenon has been established already in the linear spectra of magnetoexcitons in GaAs and other semiconductors with zinc-blende crystal structure.[31]

In Secs. V C–V E we focus on the intensity of the MFISH signal and on its dependence on magnetic field and temperature.

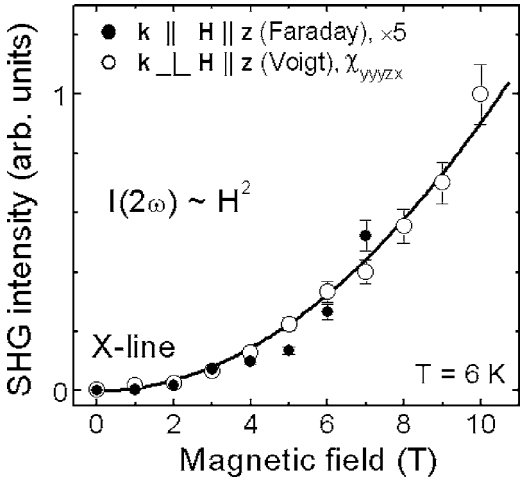

FIG. 7. MFISH intensity of the *X*-line in GaAs as function of magnetic field in Faraday and Voigt geometries. Experimental data are shown by symbols. Intensities are normalized as the signal in the Voigt geometry is by a factor of five more intense than that in the Faraday geometry. The solid line is a H^2 fit to the data.

C. Magnetic field dependence of MFISH intensity

The increase of the MFISH intensity of the strongest *X*-line with increasing *H*, is shown in Fig. 7 for the Faraday (full circles) and the Voigt (open circles) geometry. For both geometries, a quadratic dependence of the MFISH intensity on magnetic field strength is found, as demonstrated by the H^2 fit to the experimental data given by the solid line. The intensity of the SHG signal is proportional to the square of the nonlinear polarization, i.e., $I(2\omega) \propto |\mathbf{P}(2\omega)|^2$. Therefore, the nonlinear polarization $P(2\omega)$ depends linearly on *H*, a result that is in good agreement with the conclusions of our phenomenological approach in Eqs. (7) and (12). This characteristic dependence for the MFISH signals due to the orbital quantization of electronic states has been reported recently.[18] It will be discussed below along with the rotational anisotropy for the nonlinear tensor components in the Voigt geometry.

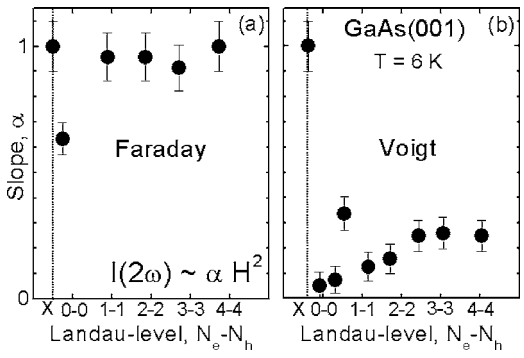

FIG. 8. Slope α of the quadratic dependence of the MFISH intensity of different observed lines on magnetic field $I(2\omega) \sim \alpha H^2$ vs Landau-level transitions N_e-N_h. Results are taken from the experimental data for the Faraday geometry in Fig. 5 and for the Voigt geometry in Fig. 6. For each panel data are normalized to the α value for the *X*-line.

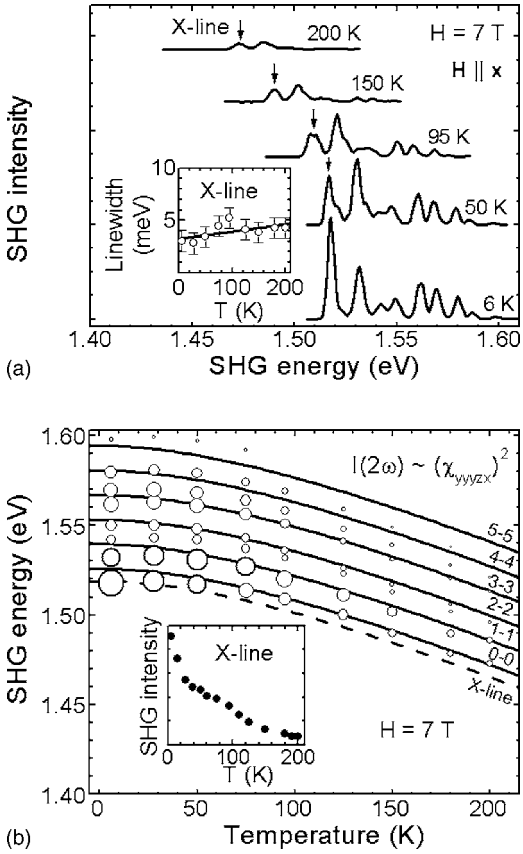

FIG. 9. (a) MFISH spectra of GaAs at different temperatures (Voigt geometry). (b) MFISH peak energies vs temperature. Circles are experimental data with symbol sizes scaled by the MFISH intensity. Solid lines present optical transition energies between Landau-levels calculated by Eq. (20) for $N_e=N_h$ at $H=7$ T combined with the temperature dependence of the GaAs band gap.[34] The integrated MFISH intensity of the *X*-line vs temperature is given in the inset.

Figure 8 shows the slope α of the quadratic dependence of the MFISH intensity on the magnetic field $I(2\omega) \sim \alpha H^2$ for several lines related to the transitions *X*, 0−0, 1−1, 2−2, 3−3, and 4−4 in the Faraday and Voigt geometries. The slopes have been obtained from fits to the experimental data presented in Figs. 5 and 6. In the Faraday geometry, the slope does not vary significantly with the Landau-level quantum number and it has the same value as for the *X*-line, with exception of the first Landau-level transition (0−0). In contrast, the α value of the *X*-line in the Voigt geometry exceeds significantly the slopes of all other transitions. Furthermore, one can see the tendency of an increase of the slope for higher Landau-level transitions. In the following, the *X*-line will be studied as an example for the whole set of observed lines.

D. Temperature dependence of MFISH signal

The MFISH signal is rather robust against a temperature variation and can be detected up to 200 K [see Fig. 9(a)]. With increasing temperature, the MFISH lines lose intensity and shift to lower energies. Surprisingly, the thermal broadening of the lines is very weak as illustrated by the inset.

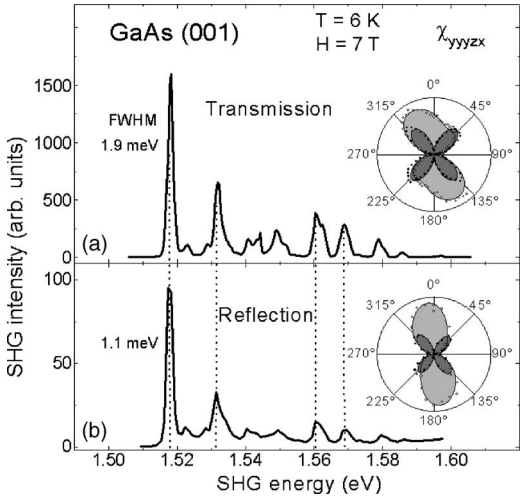

FIG. 10. MFISH spectra in (a) transmission geometry $\mathbf{k}(\omega)\|\mathbf{k}(2\omega)\|\mathbf{z}$ and (b) reflection geometry $-\mathbf{k}(\omega)\|\mathbf{k}(2\omega)\|\mathbf{z}$. In both cases, the polarization geometry was $\mathbf{E}(2\omega)\|\mathbf{E}(\omega)\|y$ (χ_{yyyzx}). The ordinate gives the MFISH intensity in arbitrary units, but the ratio of intensities is relevant for both geometries. The insets show the corresponding rotational anisotropies.

The dominant mechanism responsible for the shift of the MFISH lines is the temperature decrease of the GaAs band gap. This is confirmed by Fig. 9(b), where the MFISH peak positions are compared to the expected temperature shifts of the 1*s*-exciton and the Landau-level transitions.

The dependence of the integrated intensity of the 1*s*-exciton (*X*-line) on temperature is given in the inset of Fig. 9(b). The decrease of the MFISH intensity cannot be described by a monoexponential form, and therefore, no specific activation energy can be identified. One of the possible mechanisms for the temperature dependence is carrier-phonon scattering, which perturbs the cyclotron motion of free carriers and, therefore, the orbital quantization. Scattering causes a considerable broadening of excitonic lines in linear optical spectra. This is definitely not the case for the MFISH spectral lines as shown by the inset in Fig. 9(a). We suggest that this difference comes from the coherence of the SHG process. The temperature stability of the MFISH line width may be explained analogously to that of the x-ray Bragg scattering at a crystal lattice. Thermal motion of the atoms leads to a decrease of the x-ray signal intensity, which is described by the Debye-Waller factor in the case of Bragg scattering.[35] The line width, however, remains constant due to the fact that signal contributions from different unit cells interfere constructively only if the constraints due to the Laue equations are fulfilled.

E. Transmission vs reflection geometry

Because GaAs is transparent at the fundamental frequency ($\hbar\omega < E_g$), absorption occurs only for SHG light above the band gap ($2\hbar\omega > E_g$). In this case, the transmission geometry $\mathbf{k}(\omega)\|\mathbf{k}(2\omega)\|\mathbf{z}$ can be used for SHG studies. Nevertheless for materials, which possess absorption even at

the fundamental frequency, the reflection geometry $-\mathbf{k}(\omega)\|\mathbf{k}(2\omega)\|\mathbf{z}$ is an alternative since the same selection rules as for transmission are valid and thus the same rotational anisotropy, as calculated above, is expected.

Figure 10 compares MFISH spectra for transmission and reflection geometry. In both cases, the MFISH spectra are very similar with respect to the spectral positions of the observed peaks as well as their relative peak intensities. The only difference is that the MFISH intensity in the reflection geometry is by an order of magnitude weaker than that in transmission.

This can be explained by a phase matching effect. The SHG intensity usually scales inversely with the wave-vector difference of fundamental and SHG light: $I(2\omega)^{\mathrm{SHG}} \propto 1/|2\mathbf{k}(\omega)-\mathbf{k}(2\omega)|$. This wave-vector mismatch is much larger for counterpropagating beams in the reflection geometry than for coparallel propagating beams in transmission geometry. Another possible origin is that in the reflection geometry the MFISH is generated mainly by the fundamental beam reflected from the back facet of the sample. Therefore, the pump power converted into SHG signal is considerably reduced, which will cause even stronger increase of the signal intensity due to nonlinear origin of MFISH.

The observed line widths of the *X*-line are of comparable magnitude (1–2 meV) and close to the experimental resolution limit. The rotational anisotropies for transmission and reflection also do not differ significantly as shown by the insets in Fig. 10. In the following, only the transmission geometry will be considered due to the higher MFISH intensity.

VI. ROTATIONAL ANISOTROPY AND MAGNETOSPATIAL DISPERSION

In this section, the characteristic polarization properties of the experimental MFISH data will be discussed to show that the electric-dipole approximation is not sufficient for modeling the rotational anisotropy and further terms have to be considered. Also the spectral dependencies of the different tensor components will be analyzed as a function of magnetic field.

MFISH spectra measured in different polarization and magnetic field geometries at normal light incidence are shown in Fig. 11. The applied magnetic field induces SHG signals consisting of a set of narrow lines in the spectral range of 1.51–1.70 eV. Here, an extended energy range is displayed compared to the data in Figs. 5 and 6. First, only the Voigt geometry spectra [Figs. 11(a)–11(c)] will be discussed. Their comparison to the Faraday geometry data will be given in Sec. VII.

High spectral resolution (<1 meV) was reached by using a narrow monochromator slit leading to reduced MFISH intensity and, therefore, to a decreased signal-to-noise ratio. MFISH signals measured for $\mathbf{E}(2\omega)\perp\mathbf{E}(\omega)$ are shown in Figs. 11(a) and 11(b). In this configuration, MFISH is allowed in the electric-dipole approximation Eq. (7). In Fig. 11(a), it is purely given by the fourth-rank tensor component χ_{xyyx}. For Fig. 11(b), it can be explained by contributions of the two tensor components χ_{xyyx} and χ_{yxyx}. The signal measured for $\mathbf{E}(2\omega)\|\mathbf{E}(\omega)$ is shown in Fig. 11(c) and corresponds to the χ_{yyyx} electric-dipole component. This component, however, is forbidden. It becomes allowed taking into account the spatial-dispersion, which gives an MFISH contribution χ_{yyyzx} in the fifth-rank susceptibility tensor. Surprisingly, the MFISH intensity due to this χ_{yyyzx} component is 50 times larger than that due to the electric-dipole allowed χ_{xyyx} component. This confirms that the electric-dipole approximation is insufficient and the magnetospatial dispersion given by Eq. (12) is required for an adequate description of the MFISH signals.

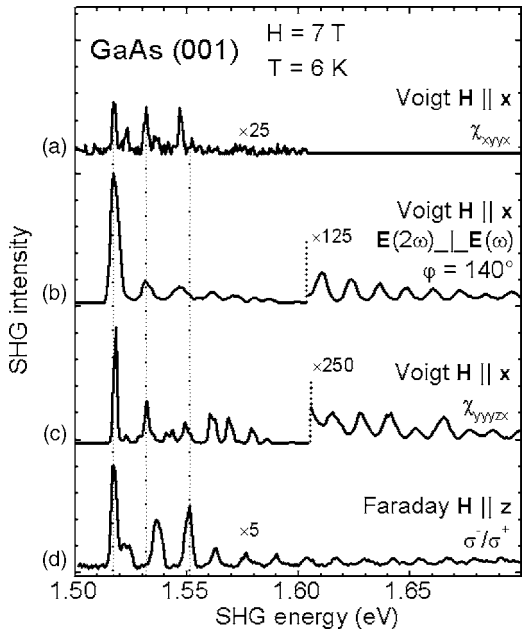

FIG. 11. MFISH spectra in GaAs for $\mathbf{k}(\omega)\|\mathbf{z}$ and different magnetic field orientations. In the Voigt geometry both fundamental and SHG light are linearly polarized. The considered SHG cases are (a) Electric-dipole component χ_{xyyx} $[\mathbf{E}(2\omega)\perp\mathbf{E}(\omega)\|\mathbf{y}]$, (b) Polarization geometry $\mathbf{E}(2\omega)\perp\mathbf{E}(\omega)$ with $\varphi=140°$, resulting in an interference of all five tensor components, and (c) spatial-dispersion component χ_{yyyzx} $[\mathbf{E}(2\omega)\|\mathbf{E}(\omega)\|\mathbf{y}]$. In the Faraday geometry shown by trace (d), σ^- circularly polarized light is used for excitation and σ^+ polarized MFISH is detected. The ordinate in each case gives the MFISH intensity in arbitrary units, but the ratio between the scales for the different geometries is relevant.

Next, the characteristic rotational anisotropy for different MFISH lines will be considered. Thereby the information about the underlying nonlinear optical processes is detailed further. The MFISH intensities shown in Fig. 12 are given as a function of the angle φ between the polarization plane of the fundamental light and the crystallographic axis [010] for the $\mathbf{E}(2\omega)\|\mathbf{E}(\omega)$ and $\mathbf{E}(2\omega)\perp\mathbf{E}(\omega)$ geometries.

The rotational anisotropy of the MFISH signal features diverse twofold patterns that cannot be explained using only the electric-dipole approximation leading to the rotational anisotropy of Eqs. (9) and (10) and shown exemplarily by Fig. 12(e). We come here again to the conclusion that the magnetospatial dispersion mechanisms, allowing the fifth rank tensor component χ_{yyyzx}, is of great importance for the MFISH signals in GaAs.

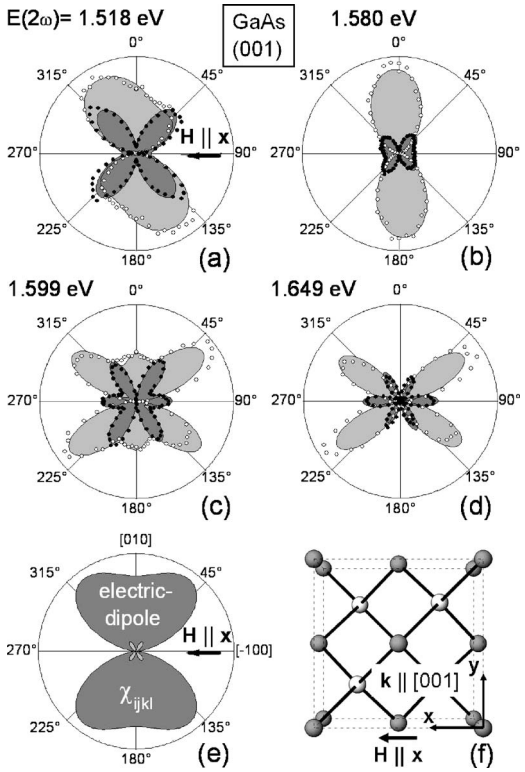

FIG. 12. MFISH rotational anisotropy in GaAs for geometries $\mathbf{E}(2\omega)\|\mathbf{E}(\omega)$ (light shaded areas and open circles) and $\mathbf{E}(2\omega)\perp\mathbf{E}(\omega)$ (dark shaded areas and filled circles) measured at $T=6$ K for $H=7$ T. The experimental data are given by circles and the shaded areas represent simulations using Eqs. (15) and (16). Note that a proper description cannot be achieved in the electric-dipole approximation Eqs. (9) and (10) in (e). (f) shows the crystal orientation in the experiment.

The experimental data in Fig. 12 were fitted using Eqs. (15) as well as (16) and by taking into account that the nonlinear optical susceptibilities are complex numbers. Note that the real and imaginary parts of the nonlinear susceptibility may vary strongly with the parameters of experiment (e.g., magnetic field strength, photon energy, and temperature). This would lead, in turn, to strong changes in the shape of the rotational anisotropy. A Fortran program based on a modified Marquardt procedure[36] was used to fit the experimental data at each photon energy. The results of this computation are given in Figs. 12(a)–12(d) by the shaded areas. Good agreement between experimental and calculated MFISH intensities is found for all rotational anisotropies. This indicates that an approach, which includes both electric-dipole and magnetospatial dispersion contributions, is sufficient to describe the whole variety of the observed MFISH signals.

A. Spectral dependence

In this section the fitting procedure as well as the physical meaning of the fitting parameters will be discussed in more detail.

Because the components of the nonlinear susceptibility tensors χ_{xyyx}, χ_{yxyx}, χ_{yxxzx}, χ_{yyyzx}, and χ_{xxyzx} are complex numbers, a set of ten fitting parameters is available. One of the parameters [here: $\mathrm{Im}(\chi_{xxyzx})=0$] can be fixed, which corresponds to a certain choice for the phase of the complex parameter set. Unfortunately, the remaining set of nine parameters depends on the starting values used in the fitting procedure. Thus, the set of fitting parameters is not unique and cannot be attributed to the real and imaginary parts of the nonlinear susceptibility. However, the moduli of the three tensor components ($|\chi_{xyyx}|$, $|\chi_{yxxzx}|$, and $|\chi_{yyyzx}|$) are determined uniquely by this fitting procedure. An alternative possibility is to measure these values directly from the MFISH intensity for $\varphi=0°$, 90° as can be seen from Eqs. (17)–(19). This procedure leads to the same values of the tensor components as determined by fitting. No direct access to the moduli of the tensor components $|\chi_{yxyx}|$ and $|\chi_{xxyzx}|$ is possible, since these components cannot be probed separately as $\varphi\neq 0°$, 90° is required to obtain their contributions. However, for $\varphi\neq 0°$, 90° all tensor components contribute and an interference of the imaginary and real parts of these components occurs [Eqs. (15) and (16)].

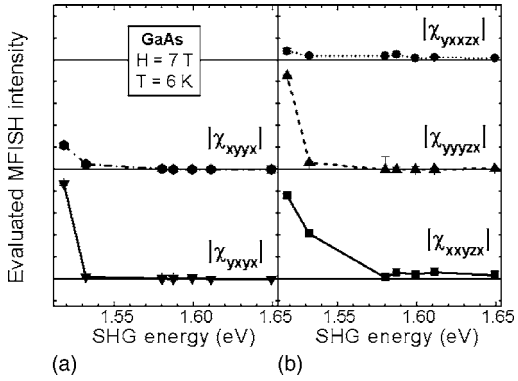

FIG. 13. Spectral dependence of the MFISH intensity evaluated for different MFISH tensor components in GaAs: (a) electric-dipole components of χ_{ijkl} type and (b) magnetospatial dispersion components of χ_{ijklm} type.

The set of tensor component moduli obtained by fitting is given in Fig. 13 in terms of the calculated MFISH intensities contributed solely by each component. It is plotted as a function of the SHG energy. Figure 13(a) shows the evaluated MFISH intensity for electric-dipole components $I_{ev}(\chi_{ijkl})$ described by a fourth-rank tensor, whereas Fig. 13(b) gives the magnetospatial dispersion components $I_{ev}(\chi_{ijklm})$ described by a fifth-rank tensor. Strong changes of the slopes close to the GaAs band gap at 1.519 eV and a continuous decrease with increasing MFISH energy are seen for all parameters. The reasonable magnitude of the error bars indicates the reliability of the fitting procedure.

B. Magnetic field dependence

The magnetic field dependence of the MFISH intensity described by the tensor component χ_{yyyzx} shown in Fig. 7, was discussed in Sec. V C. Here we discuss the magnetic field dependence of the MFISH signal for different polarization geometries. Figure 14(a)–14(c) gives the rotational anisotropy pattern for different magnetic fields. In the follow-

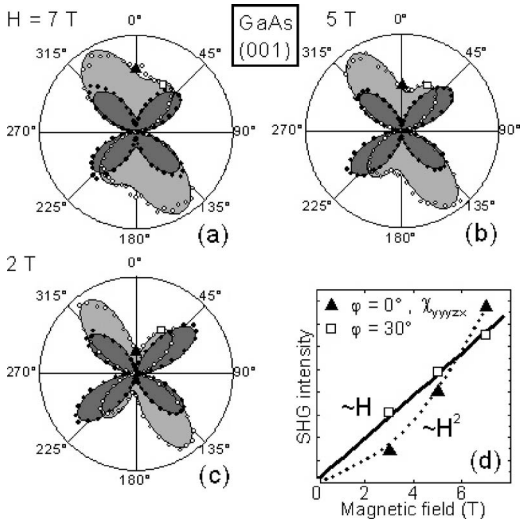

FIG. 14. MFISH rotational anisotropy of the X-line in GaAs measured at $T=6$ K. In (d), specific polarization geometries are chosen to determine the MFISH intensity dependence of $I(2\omega)_{\parallel}^{\mathrm{MFISH}}(\varphi=0°)\propto|\chi_{yyyzx}|^2$ (triangles) and $I(2\omega)_{\parallel}^{\mathrm{MFISH}}(\varphi=30°)$ (squares) on magnetic field.

ing, specific polarizations are considered in order to explain the complex polarization dependence of the MFISH signal. In Figs. 14(a)–14(c), triangles give the MFISH contribution of $I(2\omega)_{\parallel}^{\mathrm{MFISH}}(\varphi=0°)\propto|\chi_{yyyzx}|^2$, whereas data given by squares display the result of interference of all five tensor components $I(2\omega)_{\parallel}^{\mathrm{MFISH}}(\varphi=30°)$, according to Eq. (15). Figure 14(d) gives the magnetic field dependence of the MFISH intensity for these polarization geometries. In the case of $\varphi=0°$, a quadratic dependence on magnetic field is found for the MFISH intensity, whereas for $\varphi=30°$, surprisingly, a linear dependence is revealed. In principle, the linear dependence of the SHG intensity on the magnetic field may result from a cross term originated by interference between field-dependent and field-independent terms. Such a behavior has been reported in Ref. 37. However, in our case such interference is not obvious as no field-independent terms are recognized at $H=0$ T.

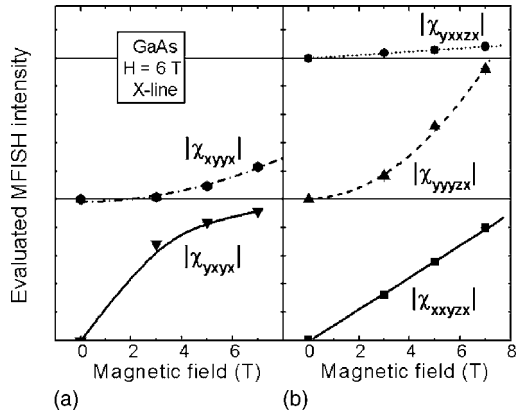

FIG. 15. Magnetic field dependence of the MFISH intensity evaluated for different MFISH tensor components in GaAs for the X-line at $T=6$ K: (a) electric-dipole components of χ_{ijkl} type and (b) magnetospatial dispersion components of χ_{ijklm} type.

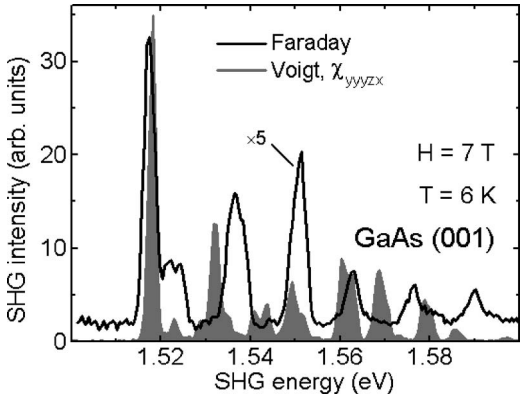

FIG. 16. MFISH spectra in GaAs. In the Faraday geometry circularly σ^- polarized light was chosen for excitation and σ^+ polarized MFISH was detected (intensity is multiplied by a factor of 5). For comparison, the MFISH contribution χ_{yyyzx} in the Voigt geometry using linear polarizations is given by the shaded area.

In order to explain this linear dependence, the MFISH intensities evaluated from the moduli of the tensor components obtained by the fitting procedure can be considered. They are shown in Fig. 15. The component $|\chi_{yxxzx}|$ is rather weak and thus the evaluated MFISH intensity $I_{ev}(\chi_{yxxzx})$ can be neglected. The specific field dependence found for $I_{ev}(\chi_{yxyx})$ as well as the linear dependence for $I_{ev}(\chi_{xxyzx})$ can be explained as follows. For $\varphi\neq0°$, 90°, the MFISH intensity is determined by a complex interference of all tensor components. Therefore, the fitting procedure does not result in a unique set of parameters, so that the tensor components χ_{yxyx} and χ_{xxyzx} and thus $I_{ev}(\chi_{yxyx})$ and $I_{ev}(\chi_{xxyzx})$ cannot be determined uniquely. One of the combinations for these components, which allows one to describe the rotational anisotropies, is shown in Fig. 15. In contrast, the modulus of tensor components $|\chi_{xyyx}|$ and $|\chi_{yyyzx}|$ can be determined uniquely, as can be seen from Eqs. (19) and (17). For both components, the evaluated MFISH intensities show a quadratic behavior on the magnetic field, in accordance with Eqs. (7) and (12) and the macroscopic model, which predicts $I(2\omega)^{\mathrm{MFISH}}\propto H^2$.

VII. COMPARISON OF FARADAY AND VOIGT GEOMETRIES

A. MFISH spectra

MFISH spectra obtained in the Faraday geometry with circularly polarized light (line) and the Voigt geometry with linearly polarized light (shaded area) are compared in Fig. 16. This comparison reveals several important differences.

The MFISH intensity in the Voigt geometry is found to be by a factor of five stronger. This is not surprising, as the tensor components of the nonlinear susceptibility are symmetry forbidden for the Faraday geometry (see Sec. II) and cannot be described on the basis of Eqs. (7) and (12).

One can clearly see in Fig. 16 a strong background signal in the Faraday geometry, whereas this is not observed in the Voigt geometry. We attribute it to residual crystallographic SHG. This may provide one of the possible explanations for

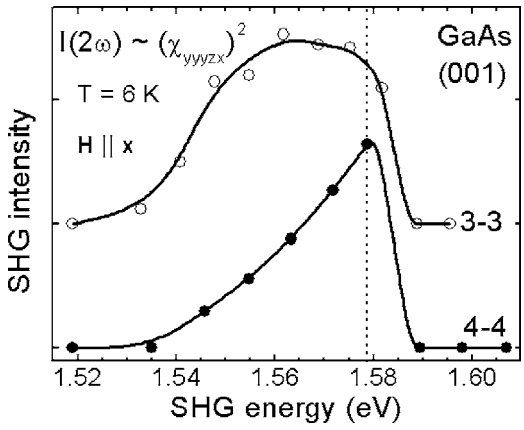

FIG. 17. Spectral dependence of the MFISH intensity described by χ_{yyyzx} for different Landau-levels in the Voigt geometry. The MFISH signal increases with the MFISH energy of the corresponding Landau level transition N_e-N_h (e.g., 3-3, 4-4), which was tuned by varying the magnetic field. Above 1.58 eV, however, the MFISH intensity decreases rapidly, irrespective of the transition.

the observation of relatively strong MFISH signal in the Faraday geometry. Interference of crystallographic with magnetic background SHG may explain the observed MFISH for the Faraday geometry.

Another possible explanation is the following: The magnetic field lifts the spin degeneracy of the Landau levels and induces spin quantization, which is characterized by the spin splitting $\mu_B(g_e+g_h)H$. Here μ_B is the Bohr magneton and $g_{e(h)}$ are the g factors of the conduction band electrons and valence band holes. Even though the spin splitting is small, not exceeding 1 meV up to 10 T, it might contribute to MFISH in the Faraday geometry because the spin inversion symmetry is broken. This mechanism is similar to the MFISH process reported for diluted magnetic semiconductors featuring a giant Zeeman splitting.[18] For a description of the MFISH process in the Faraday geometry, the additional spin degree of freedom would have to be taken into account.

Spectra in the Voigt geometry feature more lines and their peak energies differ from those in the Faraday geometry. This originates from the symmetry of the conduction and valence band states and its modification for the different configurations of applied magnetic field and light wave vector. A detailed discussion is given in Sec. VII B.

The amplitude of the MFISH lines decreases with increasing energy for both field orientations; however, the character of the decrease is qualitatively different. As can be seen from Fig. 11 (showing an extended energy range up to 1.70 eV), the MFISH spectrum (d) for the Faraday geometry shows a smooth intensity decrease within the whole energy range. A remarkable feature of the Voigt geometry is an abrupt decrease of intensity between 1.58 and 1.59 eV. In Figs. 11(b) and 11(c), this is shown for $H=6$ T and can be followed also in the fan chart of Fig. 6(b). The drop is indeed linked to a certain spectral energy and not to specific Landau levels, which pass this energy with increasing magnetic field. To illustrate that, the intensity of the 3–3 and 4–4 MFISH lines in the Voigt geometry are plotted in Fig. 17. The strong decrease above 1.58 eV has been established for all MFISH tensor components. A possible explanation for this cutoff energy at 1.59 eV might be optical-phonon scattering. The energy difference between this cutoff energy and the GaAs band gap (or 1s-exciton ground state) is ~70 meV, which is rather close to the energy of two optical phonons of $2\times\hbar\omega_{LO}=2\times36.6$ meV.[34]

B. Fan charts

In contrast to the good description of the MFISH signal in the Faraday geometry by the model of Landau-levels [see Fig. 5(b)], this model is not sufficient to explain the MFISH signal in the Voigt geometry [see Fig. 6(b)]. In general, the Coulomb interaction between electrons and holes would have to be taken into account, which complicates the Landau-level diagram leading to a rich fan chart of magnetoexcitons.[31] Opposite to the Coulomb interaction, which possesses a spherical symmetry, the Landau-level quantization features the symmetry of a cylinder with the axis defined by the magnetic field. Consequently, no exact mathematical solution including both interactions can be formulated for the exciton. Instead, approximations for the limits of low and high magnetic fields have to be considered. In the case of low magnetic fields $\hbar\omega_c \ll R$, where ω_c is the cyclotron frequency and R is the exciton binding energy (exciton Rydberg), the Coulomb interaction dominates over the magnetic confinement, and gives $R \geqslant 4.2$ meV for the 1s exciton and $\geqslant 1$ meV for the binding energy of the 2s-exciton in GaAs. The magnetic field can be considered by perturbation theory, leading to a diamagnetic shift $\propto H^2$. In the case of high magnetic fields $\hbar\omega_c \gg R$ the Landau-level quantization, which is characterized by a cyclotron energy of $\hbar\omega_c^e \approx 1.75$ meV/T for the electron states, prevails. The Coulomb interaction now has to be treated by perturbation theory. Both descriptions are not suitable in the magnetic field range of a few Tesla, where $\hbar\omega_c \sim R$. In this case, the magnetoexcitons reveal a complicated level structure already in linear absorption experiments.[31] An even richer spectrum is expected for the MFISH process involving three photons, which results in higher flexibility in the selection rules to fulfill angular momentum conservation. Therefore, additional optical transitions, which are inactive in linear spectroscopy, may become allowed.

A possible explanation for the different fan charts in the Voigt and the Faraday geometry is the following. The bulk crystal has no intrinsic preferential direction. Such directions are introduced by the experiment: (a) by the magnetic field orientation and (b) by the propagation direction of the fundamental light. In the Faraday geometry, these two directions coincide and only one preferential direction is present. The Landau-level orbital movement of the carriers is perpendicular to $\mathbf{k}(\omega)$ and occurs, therefore, in-plane of the light polarizations. In contrast, in the case of the Voigt geometry two axes, which are perpendicular to each other, $\mathbf{H}\|\mathbf{x}$ and $\mathbf{k}(\omega)\|\mathbf{z}$, are involved. Therefore the Landau orbital movement occurs in a plane, in which also the light propagation is located, which represents a geometry with lowered symmetry. Then more complex SHG selection rules may be expected leading to a richer magnetoexciton spectrum [see Fig. 6(b)].

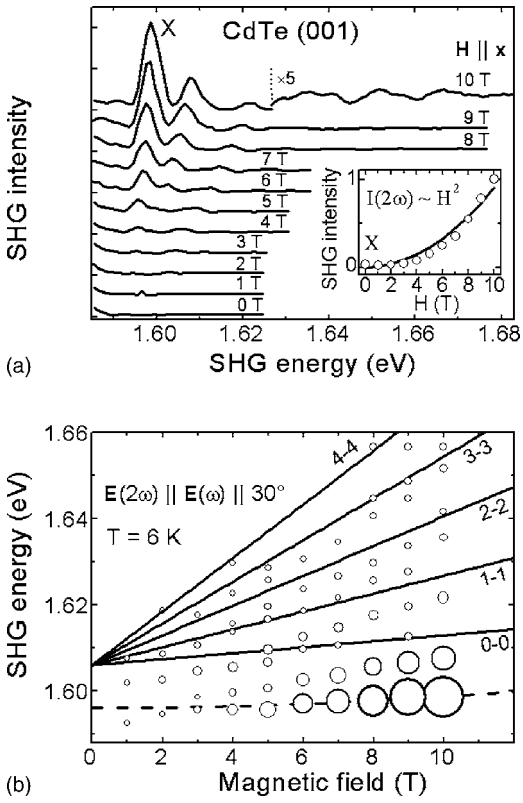

FIG. 18. (a) MFISH spectra of CdTe at different magnetic fields in Voigt geometry for $T=6$ K. The inset shows the integrated intensity of the strongest X-line vs magnetic field. The solid line is a H^2-fit to the data. (b) Landau-level fan chart diagram of the MFISH peak positions: circles are experimental data with intensities given by the symbol size. Solid lines give optical transitions between Landau-levels calculated from Eq. (20) for $N_e=N_h$. The dashed line gives literature data for the diamagnetic shift of the $1s$-exciton state.

Note that the strongest component observed in the Voigt geometry is χ_{yyyzx} (Fig. 15), for which the polarizations of all light waves are parallel to the y axis. The y axis is in the plane of the orbital motion caused by $\mathbf{H}\|\mathbf{x}$. In this case, the polarizations can only couple to the motion of the carriers along the y axis but not along the z axis since $\mathbf{k}(\omega)\|\mathbf{z}$. In accordance with the previous argumentation, no χ_{xxxzx} MFISH signal is observed for which the polarizations of the light waves are parallel to the magnetic field $\mathbf{H}\|\mathbf{x}$ [see $I(2\omega)_{\|}^{\mathrm{MFISH}}(\varphi=90°)$ in Figs. 12(a)–12(d)]. Strong MFISH contributions are also found if the polarization of either the MFISH or the fundamental light wave has a component in the plane of the orbital motion [see $I(2\omega)_{\|}^{\mathrm{MFISH}}(\varphi=0°)$, $I(2\omega)_{\perp}^{\mathrm{MFISH}}(\varphi=0°)$, or $I(2\omega)_{\perp}^{\mathrm{MISH}}(\varphi=90°)$, in Figs. 12(a)–12(d)]. This clearly indicates that the MFISH couples to the orbital motion of carriers, and therefore, orbital quantization plays a key role in its generation.

VIII. MAGNETIC-FIELD-INDUCED SHG IN CdTe

Thus far, the MFISH process was discussed for the III-V semiconductor GaAs. In order to prove the general nature of the observed phenomena, the II-VI semiconductor CdTe was chosen for further studies. The MFISH data are found to be very similar to those observed in GaAs: Fig. 18(a) shows MFISH spectra of CdTe in the Voigt geometry. In magnetic field, the SHG signal appears consisting of a set of narrow lines in the spectral range from 1.59 to 1.67 eV. With increasing field, these lines shift to higher energies and gain in intensity. The intensity increase is proportional to H^2 as can be seen from the corresponding fit to the data for the strongest X-line in the inset. This behavior is similar to that of GaAs (see Fig. 7). The X-line width is <4 meV and independent of magnetic field.

The fan chart of MFISH lines is given in Fig. 18(b). Similarly to GaAs, these lines can be assigned to magnetoexciton states. At zero magnetic field, it starts from 1.596 eV, which is the $1s$-exciton energy in CdTe at $T=6$ K. The diamagnetic shift of the $1s$-exciton state[31] given by the dashed line follows well the X-line. The solid lines in Fig. 18(b), which correspond to optical transitions between Landau levels, are calculated using Eq. (20) with the following parameters for CdTe at $T=6$ K: $E_g=1.606$ eV, $m_e^*=0.096m_0$, and $m_{hh}^*=0.674m_0$.[34] The exciton spin splitting, which does not exceed 0.1 meV below 10 T, is not taken into account.

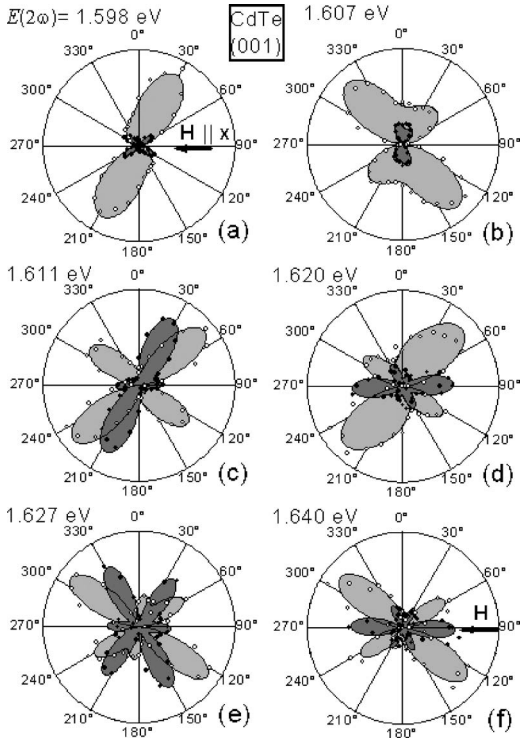

FIG. 19. MFISH rotational anisotropy in CdTe for geometries $\mathbf{E}(2\omega)\|\mathbf{E}(\omega)$ (light shaded areas and open circles) and $\mathbf{E}(2\omega)\perp\mathbf{E}(\omega)$ (dark shaded areas and filled circles) at $T=6$ K and $H=10$ T. Experimental data are given by circles and shaded areas represent simulations using Eqs. (15) and (16).

The MFISH intensities shown in Fig. 19 are given as function of the angle φ between the polarization of the fundamental light and the crystallographic [010] axis for the $\mathbf{E}(2\omega)\|\mathbf{E}(\omega)$ and $\mathbf{E}(2\omega)\perp\mathbf{E}(\omega)$ geometries [see the scheme in Fig. 12(f), which is identical for GaAs and CdTe due to the same crystal symmetry]. Similar to GaAs, the rotational

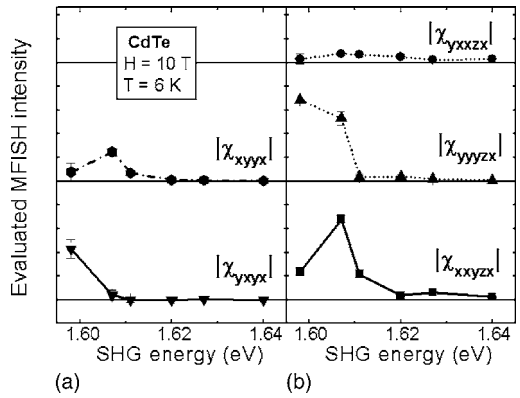

FIG. 20. Spectral dependence of the MFISH intensity evaluated for different MFISH tensor components in CdTe obtained by fitting: (a) electric-dipole components of χ_{ijkl} type and (b) magnetospatial dispersion components of χ_{ijklm} type.

anisotropy of the MFISH signal features complicated twofold patterns.

The MFISH rotational anisotropy has been simulated using Eqs. (15) and (16). Figure 20 shows the spectral dependence of the MFISH intensities calculated for the moduli of the tensor components obtained from the fit. As in GaAs (see

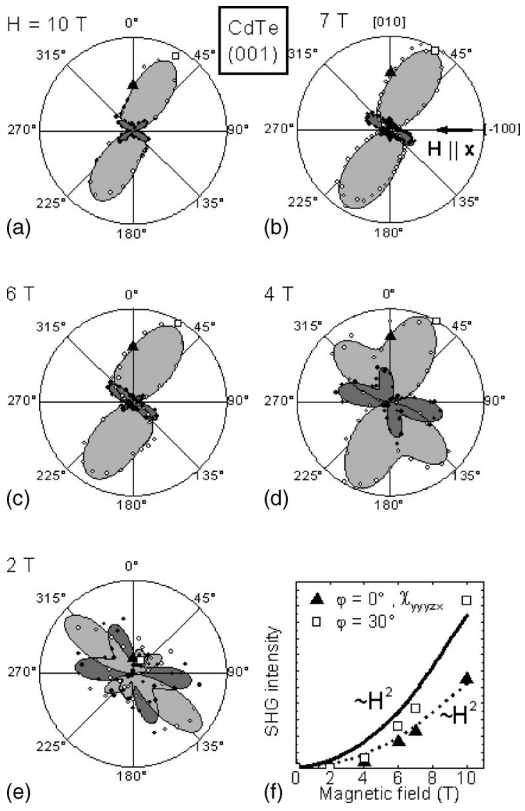

FIG. 21. MFISH rotational anisotropy of the *X*-line in CdTe at $T=6$ K for different magnetic fields. In (a)–(e), the signal is detected in geometries $\mathbf{E}(2\omega)\|\mathbf{E}(\omega)$ (light shaded areas and open circles) and $\mathbf{E}(2\omega)\perp\mathbf{E}(\omega)$ (dark shaded areas and filled circles). (f) Specific polarization geometries were chosen to determine the MFISH intensity dependence of $I(2\omega)_{\|}^{\mathrm{MFISH}}(\varphi=0°)\propto|\chi_{yyyzx}|^2$ (triangles) and $I(2\omega)_{\|}^{\mathrm{MFISH}}(\varphi=30°)$ (squares) on magnetic field.

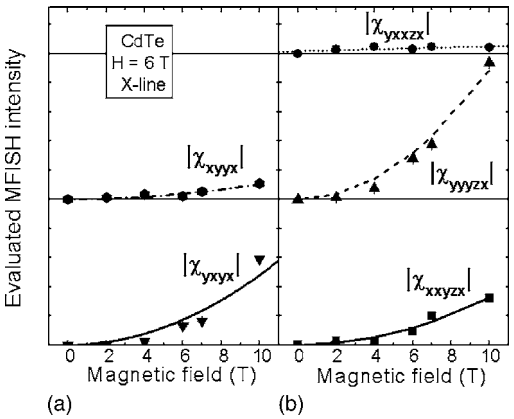

FIG. 22. Magnetic field dependence of the MFISH intensity evaluated for different MFISH tensor components in CdTe for the *X*-line at $T=6$ K: (a) electric-dipole components of χ_{ijkl} type, (b) magnetospatial dispersion components of χ_{ijklm} type. Note that in contrast to the GaAs case (Fig. 15), the MFISH intensity depends quadratically on the magnetic field for all tensor component.

Fig. 13) strong changes of the slope close to the band gap and a continuous decrease with increasing MFISH energy are observed.

However, the magnetic field dependence of the MFISH signal in CdTe shows an important difference compared to those in GaAs. Figure 21 shows the *X*-line rotational anisotropy for different magnetic fields. The field dependence of $I(2\omega)_{\|}^{\mathrm{MFISH}}(\varphi=0°)\propto|\chi_{yyyzx}|^2$ and $I(2\omega)_{\|}^{\mathrm{MFISH}}(\varphi=30°)$ is given in Fig. 21(f). For both cases, a quadratic magnetic field dependence of the MFISH intensity is found, whereas in GaAs [Fig. 14(d)] a linear field dependence had been observed for $I(2\omega)_{\|}^{\mathrm{MFISH}}(\varphi=30°)$.

Figure 22 shows that all MFISH intensities calculated for the moduli of five MFISH tensor components increase quadratically with magnetic field. Thus in CdTe, the experimental data are in full accordance with the macroscopic model described by Eqs. (7) and (12): $I(2\omega)^{\mathrm{MFISH}}\propto H^2$.

The entirety of these findings shows that the MFISH phenomena in CdTe and GaAs manifest themselves in qualitatively identical fashions. This leads us to the conclusion that similar MFISH properties can be expected for the wide class of semiconductor and insulator materials with zinc-blende crystal structure and similar band structures.

IX. CRYSTAL QUALITY

It is known that high structural perfection of the crystal is of great importance for achieving strong SHG signals. The reason lies in the coherent origin of the SHG process, with the coherence length as important parameter. The same should be true for MFISH. Indeed, during the course of this study we have recognized a strong correlation of the MFISH efficiency with the structural quality of the studied samples. In this section, we will examine two sets of samples with different approaches for "manipulating" the structural quality. The first approach concerns nominally identical GaAs crystals which were grown, however, by different methods. The main difference comes here from the density of the de-

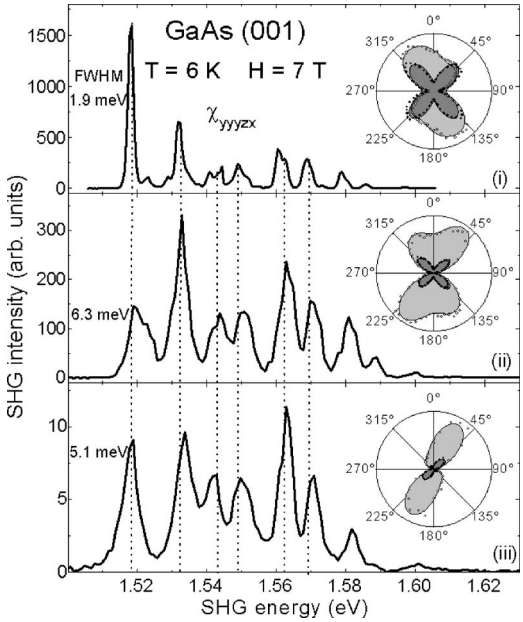

FIG. 23. MFISH spectra of GaAs samples with different structural quality: (i) 10 μm gas-phase-epitaxy layer, (ii) 2 μm epilayer grown by molecular-beam epitaxy, and (iii) 0.5 mm platelet of bulk GaAs grown by the Bridgman method.

fects (see Sec. III). The second approach exploits the concept of ternary alloys through studying $Cd_{1-x}Mg_xTe$, which is achieved from binary CdTe by isoelectronic substitution of Cd cations by Mg. This causes structural imperfections due to the inhomogeneous distribution of Mg ions in the cation sublattice. Also the optical properties are modified, e.g., the absorption edge is shifted to higher energies and broadened due to alloy fluctuations.

A. GaAs

MFISH spectra of three different GaAs samples are shown in Fig. 23. For all samples, the spectra were found to be similar with respect to the MFISH spectral line positions, although the peak intensities vary significantly. The line widths, however, differ from sample to sample. The width of *X*-line is 1.9, 6.3, and 5.1 meV for samples (i), (ii), and (iii), respectively. This trend is in good agreement with the higher density of defects in samples (ii) and (iii). With increasing linewidth the SHG intensity decreases by about two orders of magnitude. Therefore, both criteria, linewidth and intensity, indicate that sample (i) possesses the highest quality and the strongest MFISH signal.

The rotational anisotropy for the different GaAs samples is shown in the insets of Fig. 23. We attribute the difference in the anisotropy patterns to the influence of the crystal quality on the nonlinear susceptibility.

B. (Cd, Mg)Te

For this ternary alloy the structural quality is controlled by the Mg content. Figure 24 shows MFISH spectra for CdTe and $Cd_{1-x}Mg_xTe$ samples with magnesium concentrations of $x=0.01$ and 0.08. In comparison to the spectra

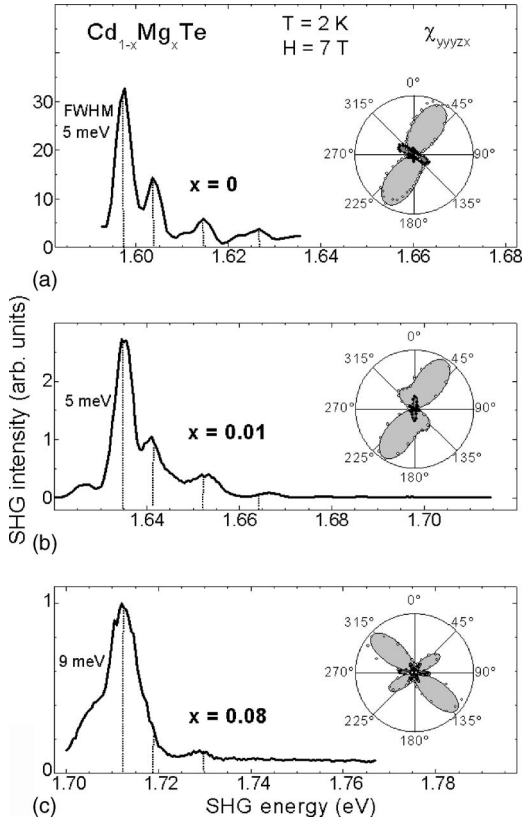

FIG. 24. Influence of the magnesium concentration on the MFISH spectra and the rotational anisotropies in $Cd_{1-x}Mg_xTe$. (a) $x=0$, CdTe; (b) $x=0.01$; and (c) $x=0.08$. Magnetic field is applied in the Voigt geometry.

shown for GaAs in Fig. 23, the magnetoexciton structure is less pronounced. In the case of $x=0.01$, the exciton states up to the $2-2$ Landau-level transition can be traced. For $x=0.08$, only lines associated with the $1-1$ transition are observable. Higher-lying transitions are broadened and not distinguishable. Therefore, the number of observable magnetoexciton transitions in SHG can serve as a criterium for the

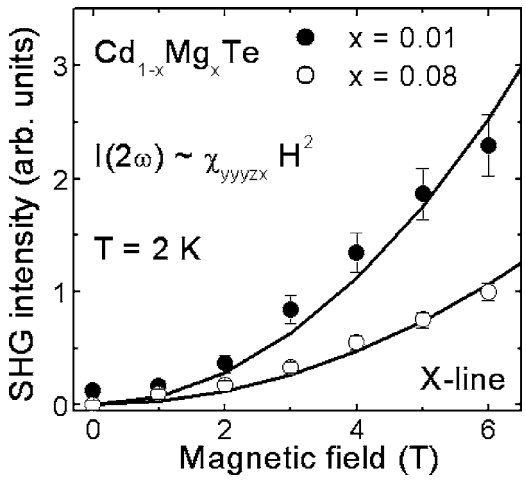

FIG. 25. MFISH intensity vs magnetic field (Voigt geometry) in $Cd_{1-x}Mg_xTe$ with $x=0.01$ and $x=0.08$. Experimental data are shown by symbols. Solid lines are H^2 fits to the data.

crystal quality. With increasing Mg concentration, the MFISH intensity decreases by a factor of 3 and the *X*-line broadens from about 5 to 9 meV.

Note that in $Cd_{1-x}Mg_xTe$ a quadratic magnetic field dependence of the MFISH intensity corresponding to the χ_{yyyzx} component is also found, which is presented for both Mg concentrations in Fig. 25.

The insets of Fig. 24 show the rotational anisotropy of the *X*-line. Strong changes of the shape of the anisotropy patterns are observed indicating strong variation of the structural quality. Obviously, the quality of the crystal, which decreases with increasing Mg concentration, strongly influences the MFISH signal.

Therefore, we have demonstrated that various parameters of the MFISH, such as signal intensity, line broadening, number of observable lines, and rotational anisotropy patterns, are very sensitive to the structural and compositional quality of the materials. This may serve as a basis for optical nondestructive methods for materials characterization.

X. CONCLUSIONS

Magnetic-field-induced SHG was studied in the diamagnetic semiconductors GaAs, CdTe, and (Cd, Mg)Te with a direct band gap. Magnetoexciton states are found to be the major features in the MFISH generation process. Therefore, orbital quantization of the electronic states is the main source of MFISH in diamagnetic semiconductors. The MFISH intensity is shown to depend quadratically on the strength of the magnetic field. Nonlinear magneto-optical spatial dispersion is revealed to be necessary for explaining the MFISH process, as only simulations of the rotational anisotropies taking into account both electric-dipole and magnetospatial dispersion contributions show a good agreement with the experimental data. Note, however, that our macroscopic analysis is purely based on symmetry considerations and does not include microscopic details of the studied materials.

A possible explanation of the involvement of higher order processes in the SHG through the application of a magnetic field is the following: The field induces an orbital quantization of free carrier states in the conduction and valence bands. This leads to a strong increase of the density of states at the discrete Landau level energies. Potentially, this might cause the enhancement of higher order contributions. These magnetospatial dispersion contributions have a characteristic length scale on the order of the light wave vector $\mathbf{k}(\omega)$.

The general nature of the MFISH phenomenon has been proved since the MFISH process is found in III-V and II-VI cubic semiconductors. We hope that the developed comprehensive set of experimental results will stimulate the development of a microscopic theory, which is required for a better understanding of the involved physical mechanisms.

ACKNOWLEDGMENTS

Samples were kindly supplied by G. Karczewski, T. Wojtowicz, J. Kossut, S. V. Ivanov, I. V. Ignatiev, and Yu. V. Zhilyaev. Valuable comments by G. Nair are appreciated. This work was supported by the Russian Foundation for Basic Research and the Program "Nanostructures." Research visits to Dortmund were financed by the Deutsche Forschungsgemeinschaft for R.V.P via Grants (No. 436RUS17/132/05 and No. 436RUS17/56/06), and for V.V.P. via Grant No. 436RUS17/71/04.

APPENDIX

In this section, the full set of allowed tensor components of the nonlinear susceptibility tensor χ_{ijklm} is given. χ_{ijklm} is described by an axial time-invariant fifth-rank tensor, which has the following nonvanishing components:[24,25]

$$
\begin{aligned}
&-\chi_{xyzxx}=\chi_{xzyxx}=\chi_{yxzyy}=-\chi_{yzxyy}=-\chi_{zxyzz}=\chi_{zyxzz}\\
&-\chi_{xyzzz}=\chi_{xzyyy}=\chi_{yxzzz}=-\chi_{yzxxx}=-\chi_{zxyyy}=\chi_{zyxxx}\\
&-\chi_{xzyzz}=\chi_{xyzyy}=\chi_{yzxzz}=-\chi_{yxzxx}=-\chi_{zyxyy}=\chi_{zxyxx}\\
&-\underline{\chi_{xyxzx}}=\chi_{xzxyx}=\chi_{yxyzy}=-\chi_{yzyxy}=-\chi_{zxzyz}=\chi_{zyzxz}\\
&-\underline{\chi_{xxyzx}}=\chi_{xxzyx}=\chi_{yyxzy}=-\chi_{yyzxy}=-\chi_{zzxyz}=\chi_{zzyxz}\\
&-\chi_{xyxxz}=\chi_{xzxxy}=\chi_{yxyyz}=-\chi_{yzyyx}=-\chi_{zxzzy}=\chi_{zyzzx}\\
&-\chi_{xxyxz}=\chi_{xxzxy}=\chi_{yyxyz}=-\chi_{yyzyx}=-\chi_{zzxzy}=\chi_{zzyzx}\\
&-\chi_{xyyzy}=\chi_{xzzyz}=\underline{\chi_{yxxzx}}=-\chi_{yzzxz}=-\chi_{zxxyx}=\chi_{zyyxy}\\
&-\chi_{xyyyz}=\chi_{xzzzy}=\chi_{yxxxz}=-\chi_{yzzzx}=-\chi_{zxxxy}=\chi_{zyyyx}\\
&-\chi_{xxxyz}=\chi_{xxxzy}=\chi_{yyyxz}=-\underline{\chi_{yyyzx}}=-\chi_{zzzxy}=\chi_{zzzyx}.
\end{aligned}
\tag{A1}
$$

The underlined tensor components denote MFISH contributions, which can be excited using the experimental geometry $\mathbf{k}\|\mathbf{z}$, $\mathbf{H}^0\|\mathbf{x}$. The other components vanish because of symmetry reasons: Because of the permutability of the two exciting photons, the components $-\chi_{xyzxx}=\chi_{xzyxx}$ in the first set of tensor components cannot be distinguished and, therefore, must vanish. For the same reason the second and third ($\chi_{xyzzz}=\chi_{xzyzz}$), fourth and fifth ($\chi_{xyxzx}=\chi_{xxyzx}$), and sixth and seventh ($\chi_{xyxxz}=\chi_{xxyxz}$) sets of tensor components are equal. Therefore, only the three excited tensor components χ_{xxyzx}, χ_{yyyzx}, and χ_{yxxzx} are independent.

[1] N. Bloembergen, *Nonlinear Optics* (Benjamin, New York, 1965).
[2] Y. R. Shen, *The Principles of Nonlinear Optics* (Wiley, New York, 1984).
[3] R. W. Boyd, *Nonlinear Optics* (Academic Press, London, 1992).
[4] *Nonlinear Optics in Metals*, edited by K. H. Bennemann (Oxford University Press, London, 1998).
[5] *Proceedings of the Topical Conference: Nonlinear Optics at Interfaces (NOPTI 1998)*, edited by E. Matthias and F. Träger [Appl. Phys. B: Lasers Opt. **68** (3) (1999)].
[6] *Proceedings of the Topical Conference: Nonlinear Optics at Interfaces (NOPTI 2001)*, edited by F. Träger [Appl. Phys. B: Lasers Opt. **74** (7-8) (2002)].
[7] J. Opt. Soc. Am. B **22**, 1 (2005), special issue on nonlinear and integrated magneto-optics, edited by A. Boardman, D. Budker, and R. Pisarev.
[8] M. Fiebig, V. V. Pavlov, and R. V. Pisarev, J. Opt. Soc. Am. B **22**, 96 (2005).
[9] H. P. Wagner, M. Kühnelt, W. Langbein, and J. M. Hvam, Phys. Rev. B **58**, 10494 (1998).
[10] S. Bergfeld and W. Daum, Phys. Rev. Lett. **90**, 036801 (2003).
[11] J. L. P. Hughes and J. E. Sipe, Phys. Rev. B **53**, 10751 (1996).
[12] S. N. Rashkeev, W. R. L. Lambrecht, and B. Segall, Phys. Rev. B **57**, 3905 (1998).
[13] B. Adolph and F. Bechstedt, Phys. Rev. B **57**, 6519 (1998).
[14] C. Klingshirn, *Semiconductor Optics* (Springer-Verlag, Berlin, 2005).
[15] W. Schäfer and M. Wegener, *Semiconductor Optics and Transport Phenomena* (Springer-Verlag, Berlin, 2002).
[16] *Landau Level Spectroscopy*, edited by G. Landwehr and E. I. Rashba (Elsevier Science, Amsterdam, 1991).
[17] R. V. Pisarev, I. Sänger, G. A. Petrakovskii, and M. Fiebig, Phys. Rev. Lett. **93**, 037204 (2004).
[18] I. Sänger, D. R. Yakovlev, R. V. Pisarev, V. V. Pavlov, M. Bayer, G. Karczewski, T. Wojtowicz, and J. Kossut, Phys. Rev. Lett. **96**, 117211 (2006).
[19] H. G. Häfele, R. Grisar, C. Irslinger, H. Wacherning, S. D. Smith, R. B. Dennis, and B. S. Wherrett, J. Phys. C **4**, 2637 (1971).
[20] V. Venkataramanan, K. Noguchi, M. Aono, and T. Suzuki, Appl. Phys. B: Lasers Opt. **74**, 683 (2002).
[21] Y. Ogawa, H. Akinaga, F. Takano, T. Arima, and Y. Tokura, J. Phys. Soc. Jpn. **73**, 2389 (2004).
[22] V. V. Pavlov, A. M. Kalashnikova, R. V. Pisarev, I. Sänger, D. R. Yakovlev, and M. Bayer, J. Opt. Soc. Am. B **22**, 168 (2005).
[23] V. V. Pavlov, A. M. Kalashnikova, R. V. Pisarev, I. Sänger, D. R. Yakovlev, and M. Bayer, Phys. Rev. Lett. **94**, 157404 (2005).
[24] R. R. Birss, *Symmetry and Magnetism* (North-Holland, Amsterdam, 1966).
[25] S. V. Popov, Y. P. Svirko, and N. I. Zheludev, *Susceptibility Tensors for Nonlinear Optics* (Institute of Physics Publishers, Philadelphia, 1995).
[26] P. S. Pershan, Phys. Rev. **130**, 919 (1963).
[27] V. N. Gridnev, V. V. Pavlov, R. V. Pisarev, A. Kirilyuk, and Th. Rasing, Phys. Rev. B **63**, 184407 (2001).
[28] Y. V. Zhilyaev, N. K. Poletaev, V. M. Botnaryuk, T. A. Orlova, L. M. Fedorov, Sh. A. Yusupova, A. Owens, M. Bavdaz, A. Peacock, B. O'Meara, and H. Helava, Phys. Status Solidi C **0**, 1024 (2003).
[29] *Handbook of Optical Constants of Solids*, Vol. 1, edited by E. D. Palik (Academic Press, San Diego, 1998).
[30] J. Jerphagnon and S. K. Kurtz, J. Appl. Phys. **41**, 1667 (1970).
[31] R. P. Seisyan and B. P. Zakharchenya, in *Landau Level Spectroscopy*, edited by G. Landwehr and E. I. Rashba (Elsevier Science, Amsterdam, 1991), Chap. 7.
[32] S. I. Gubarev, T. Ruf, M. Cardona, and K. Ploog, Phys. Rev. B **48**, 1647 (1993).
[33] L. D. Landau and E. M. Lifshitz, *Quantum Mechanics* (Pergamon Press, London, 1977).
[34] Landolt-Börnstein, *Numerical Data and Functional Relationships*, New Series, Group III, Vol. 41 A1 (Springer-Verlag, Berlin, 2001).
[35] C. Kittel, *Introduction to Solid State Physics* (Wiley, New York, 2005).
[36] J. C. Nash, *Compact Numerical Methods for Computers* (Adam Hilger, Bristol, 1979).
[37] J. I. Dadap, J. Shan, A. S. Weling, J. A. Misewich, A. Nahata, and T. F. Heinz, Opt. Lett. **24**, 1059 (1999).